



Universiteit
Leiden
Sterrewacht Leiden

LEIDEN UNIVERSITY

MASTER THESIS

Cataloging and Visualizing Cradles of Planet Formation

Author:

Ruoyan Wang

Supervisor:

Matthew Kenworthy

*A thesis submitted in partial fulfillment of the requirements
for the degree of Master of Science in Astronomy*

June 30, 2020

To mom and dad and my LHYQ

Abstract

We reconstruct circumstellar disks into 3D graphical models utilizing 2D scattered light phase functions both measured and simulated. Reproductions of surface light intensity are achieved by fitting the phase functions with two and three-component Henyey-Greenstein functions, as well as 7th order polynomials. Computed total intensity phase functions are multiplied with Rayleigh single scattering polarization to include the instrumental polarization introduced by the telescope optics. Two disk phase functions observed from HR 4796 A and HD 97048 and two simulated ones from the porous dust aggregate model are implemented to in total six disks. Among all, HD 97048 and MY lup reveal features adequately similar to the observations. A hypothesis is proposed as disks are fitted better by models with phase functions derived from other disks with similar ages, though not verified due to lack of samples and ambiguous impacts of disk properties. An online web catalog is then designed to simplify future investigations of relations between different disk parameters. Additional details to enrich the model are in demand for the next stage of development.

Contents

Abstract	i
1 Introduction	1
2 Methods	3
2.1 Database	3
2.2 Model	5
3 Discussion	7
3.1 Scattered light phase function	7
3.2 Fitting of disk features	12
3.2.1 HD 97048	12
3.2.2 Porous dust aggregate model	14
3.3 Comparing observations with models	18
3.3.1 HD 97048	18
3.3.2 Other disks	21
4 Conclusion	31
Bibliography	35

List of Figures

2.1	A screenshot of the database administration. Disk data have been migrated.	4
2.2	The cross-section of the disk skeleton. The upper and lower curves are determined by Equation 2.1. The edge of the inner disk cuts off before the origin so that the disk does not reach the central star.	5
3.1	The HG functions at different anisotropic levels. The scattered light is distributed less evenly as the g value increases.	8
3.2	Figure 3.1 in the polar coordinate.	9
3.3	Fit of the scattering phase function with a two-component HG function, with two asymmetric parameters $g_1 = 0.99_{-0.38}^{+0.01}$ and $g_2 = -0.14 \pm 0.006$, and two coefficients $w_1 = 4.0$ and $w_2 = 0.82$. This figure is reproduced with VLT/SPHERE data [1].	9
3.4	Model illustration of the scattering angle computed from the face centroid vector and camera direction vector of each facet.	10
3.5	Model illustration of the scattering angle in domination depending on observations from different regions of the disk. The inset shows the typical shape of a polarization phase curve. Together the two images reveal the relation between the expected degree of linear polarization and the location in the disk. This figure is duplicated for clarification [2].	11
3.6	Polarized and total intensity phase function obtained from the SPHERE data. Both phase functions have been normalized to their peak value. The uncertainties have been omitted for clarity. This figure is reproduced with VLT/SPHERE data [3].	12
3.7	The SPHERE total intensity phase functions fitted with various methods. A 7th order polynomial yields the best fit curve compared to both two and three-component HG functions.	13
3.8	Morphology of porous dust aggregates. Left and right panels correspond to the BCCA and BPCA models, respectively. This figure is duplicated for clarity [4].	15
3.9	Optical properties of the BCCA and BPCA models in log scale. This figure is reproduced with the data obtained from simulations using the T-Matrix and Quasi-Monte Carlo orientation averaging method [4].	15
3.10	The BCCA phase functions fitted with various methods. A 7th order polynomial yields the best fit curve compared to both two and three-component HG functions. The y-axis is log-scaled.	16
3.11	The BPCA phase functions fitted with various methods. A 7th order polynomial yields the best fit curve compared to both two and three-component HG functions. The y-axis is log-scaled.	17

- 3.12 *Left*: reduced SPHERE DPI Q_Φ (the azimuthal counterparts of the Stoke vectors Q) image of HD 97048 [3]. *Right*: the disk model reconstructed with a power-law height profile measured from HD 97048 and a color scalar set by the polarized intensity computed with observational data of HR 4796 A. The star is not included for perfect coronagrpah. *Bottom*: the total intensity phase function (blue curve) and the computed polarized intensity phase function (green curve) obtained from multiplying with the polarization efficiency (orange curve). The model is described by a two-component Henyey-Greenstein function, parametrized by the the two HG parameters, $g_1 = 0.99_{-0.38}^{+0.01}$, $g_2 = -0.14 \pm 0.006$, and the coefficients $w_1 = 4.0$ and $w_2 = 0.82$ [1]. The phase functions have been normalized to their values corresponding to the 20-degree scattering angle. 19
- 3.13 *Left*: same as in Figure 3.12. *Right*: the disk model reconstructed with a power-law height profile measured from HD 97048 and a color scalar set by the polarized intensity computed with observational data of the same disk. The star is not included for perfect coronagrpah. *Bottom*: same as in Figure 3.12, except that the phase functions are calculated using a 7th order polynomial fitted to the observation data of HD97048 [3]. The phase functions have been normalized to their peak value. 20
- 3.14 *Left*: same as in Figure 3.12. *Right*: the disk model reconstructed with a power-law height profile measured from HD 97048 and a color scalar set by the polarized intensity computed with the porous dust aggregate model. The star is not included for perfect coronagrpah. *Bottom*: same as in Figure 3.12, except that the model is described by a 7th order polynomial fitted to the BCCA type of fractal dust aggregates of the porous dust aggregate model [4]. The phase functions have been normalized to their peak value. 22
- 3.15 *Left*: same as in Figure 3.12. *Right*: the disk model reconstructed with a power-law height profile measured from HD 97048 and a color scalar set by the polarized intensity computed with the porous dust aggregate model. The star is not included for perfect coronagrpah. *Bottom*: same as in Figure 3.12, except that the model is described by a 7th order polynomial fitted to the BPCA type of fractal dust aggregates of the porous dust aggregate model [4]. The phase functions have been normalized to their peak value. 23
- 3.16 *Top*: observed image of HD 169142 at an inclination of 13 degrees. The size of the disk is measured to be 117.1 AU. *Clockwise from middle left*: same setup as the right panel of Figure 3.12, Figure 3.13, Figure 3.15, and Figure 3.14, respectively. All disk inclinations and separations have been adjusted to match with the observation. 25
- 3.17 *Top*: observed image of PDS 66 at an inclination of 30.26 degrees. The size of the disk measured to be 100.0 AU. *Clockwise from middle left*: same as Figure 3.16. 26
- 3.18 *Top*: observed image of IM lup at an inclination of 55 degrees. The size of the disk is measured to be 452.2 AU. *Clockwise from middle left*: same as Figure 3.16. 27

3.19 <i>Top:</i> observed image of MY Lup at an inclination of 77 degrees. The size of the disk is measured to be 143.9 AU. <i>Clockwise from middle left:</i> same as Figure 3.16.	28
3.20 The map of disk fitness to certain types of models. Complex aggregate models refer to those described by phase functions derived from measurements of old debris disks, while simple dust models are fitted by phase functions of young gas-rich disks. Ambiguous disk models are placed into a separate group.	29

List of Tables

3.1	Orders and corresponding coefficients of the polynomial fit to the SPHERE total intensity phase function.	14
3.2	Orders and corresponding coefficients of the polynomial fit to the BCCA total intensity phase function.	17
3.3	Orders and corresponding coefficients of the polynomial fit to the BPCA total intensity phase function.	18
3.4	Disks chosen to implement with different phase functions and to compare with the observational results. Detailed properties of each disk are obtained from various literature [5][6][7].	24

Chapter 1

Introduction

Circumstellar disks composed of dust and gas are the natural outcome of stellar formation. They are the places where planetary systems are formed through a variety of physical processes. The birth of a circumstellar disk originates from the gravitational collapse during the formation of a protostar. A molecular cloud, the cradle of newborn stars, reaches Jeans mass and begins to collapse on its gravity. As the collapsing cloud (solar nebula) condenses, random gases originally reside in the cloud move out along the direction of the nebula's net angular momentum. The conservation of angular momentum increases the rotation rate while decreasing the radius of the nebula. During this process, the centripetal acceleration from the orbital motion resists the gravitational force from the star only in the radial direction, yet the cloud remains free to collapse vertically. As a result, the cloud flattens out and forms a thin disk supported by gas pressure in the vertical direction [8]. Initially, dense gas and dust of the disk fall rapidly onto the star but, as the surrounding molecular core depletes or otherwise disperses, the accretion rate decreases and the disk preserves a small amount of mass in the form of hydrogen gas [9]. Due to the high detection rate of exoplanets and the geometry of the Solar System, these disks are generally considered protoplanetary.

Observations of optical properties are essential to astronomical studies of the circumstellar disks. For instance, since the surface temperature of a disk reveals variations depending on the distance to the star (hot near the star, cooler farther away), the radiation covers a range of wavelengths from microns to millimeters. Therefore, they can be captured with infrared (IR) and radio telescopes. Mapping the wavelength to radius lays a foundation of detailed structure modeling even with unresolved photometry [9]. Furthermore, internal friction, or viscosity, within the disk governs the prolongation of the accretion onto the star [10]. The disk loses materials through outflows and gradually spread out with time to preserve angular momentum. Meanwhile, the disk structure may also be strongly affected by photoevaporation both caused by high-intensity radiation from the central star and ultraviolet radiation from external bright stars. Moreover, the agglomeration of dust grains significantly larger than the typical sizes found in the interstellar medium (ISM) eventually grow into planetesimals with enough mass to gravitationally perturb the disk [10]. Ultimately, the disk appears with an inner hole and a gap representing a reduction in flux across a narrow range on the spectrum, which could be observed with high-resolution direct imaging.

The advent of the Infrared Astronomical Satellite (IRAS) in 1983 for the first time opened up the IR sky, allowing the conduction of the first statistical studies of disk occurrence [11][12]. Soon later the first millimeter-wavelength detector captured disks

containing large dust grains [13]. These dust grains are then determined to be filled with materials sufficiently forming planetary systems on the scale of our own Solar System [14]. Long-wavelength interferometry could resolve the rotation in the disks, but the flattened morphology of the disks was first confirmed by the optical observation, with the Hubble Space Telescope (Hubble), via highly sensitive imaging of disk shadows against a bright nebular background [15][16]. The rapid development of large telescopes in sensitivity, resolution, and wavelength coverage to a large extent enhanced astronomical observations since the new millennium. Telescopes such as The Infrared Space Observatory (ISO) and the Spitzer Space Telescope (Spitzer) have provided massive measurements of disk parameters including the mass of the central star, stellar age, surrounding environment, and evolutionary state [9]. The Submillimeter Array (SMA) has expanded the observing range into the submillimeter regime with longer baselines, allowing for detailed mapping of fainter structures [17]. Recent studies conducted using the Atacama Large Millimeter/submillimeter Array (ALMA) have started a new chapter addressing fundamental questions in circumstellar disks.

In the past five years, the largest ground-based telescopes in conjuncture with new extreme adaptive optics instruments in the optical and near-infrared (NIR) have opened new possibilities to observe these disks at high spatial resolution in scattered light. These new observations have revealed a plethora of features in these circumstellar disks from large-scale shadows (e.g. HD 142527 [18], HD 143006 [19], and HD 139614 [20]), to small rings and gaps (e.g. TW Hya [21] and HD 97048 [3]), and even huge spiral arms (e.g. HD 135344 B [22], HD 100453 A [23], and SR 21 [24]). All of these features are thought to be signposts of ongoing planet formation. Recently the first survey of such disks using the extreme adaptive optics imager Spectro-Polarimetric High-contrast Exoplanet REsearch (SPHERE) at the Very Large Telescope array (VLT) has concluded [25]. At the same time, a new program led by researchers from the University of Amsterdam and Leiden University is about to start that will significantly extend the sample of resolved disks.

We launched this project focusing on the concept of scattered light imaging. Scattered light imaging of circumstellar disks brings insight into the surface brightness, which contains crucial information regarding the optical properties of dust grains. Plenty of researches has been performed to study this subject. Assembling a complete catalog of all such observations conducted and published to date becomes a requirement in the field. Meanwhile, establishing science communications between the experts and the public has been more significant in society today. This project initiates intending to fill the gap, involve building a web interface for easy access and basic statistical analysis, along with a simplified 3D reconstruction of circumstellar disks from 2D data. The goal is on the one hand to design an efficient tool for researchers, which can be easily queried, maintained, and updated, and on the other hand a visualization experience for general audiences.

Chapter 2

Methods

This chapter introduces the modules and software used to construct the database and model. The database is designed to a dynamic web server, which allows for instant updating. The disk model is built with a 3D primitive, with the shape determined by a height profile. The disk illumination is set by a scalar color channel to show the polarization effect.

2.1 Database

The design of the database makes use of `Django`, a Python-based free and open-source web framework [26]. The database is embedded in a server-side dynamic web page whose updates are controlled by an application server processing server-side scripts. In server-side scripting, parameters determine how the assembly of every new web page proceeds, including the setting up of more client-side processing. Dynamic websites generate HTML pages by combining the content with an HTML template on the fly at the request from the user to the page. Making an update to the layout of a dynamic website is more straightforward. Directly editing the HTML template reflects the change across the website. An advantage is that this allows for the migration of massive data sets. Manually editing HTML in static websites with hundreds of lines requires an enormous amount of time and labor. Our dynamic web database includes Admin integration which implements data management as an admin action. As a result, the users can organize a list of objects selected on the change list page. [Figure 2.1](#) provides an overview of the site and data management within the administration. `Import` and `Export` functions allow users to easily manage massive amount of disk data at once. Clicking the label ranks items in alphabetical orders and enumerate them from low to high values. Double clicks will reverse the ranking. `Add Disk` function is included for users to manually add new items. `Action` refers to the onsite search bar to query items with only keywords. For security concerns, the site is protected by super usernames and passwords.

The database includes in total 12 types of parameters: object; category; spec type; r band; distance; disk major axis; inclination; RA; Dec; system age; stellar mass. Categories of circumstellar disks include T Tauri/weak-lined T Tauri (TT/wTT), debris, Herbig Ae/Be (HAe/HBe), young stellar object (YSO), transition disk (Trans), protoplanetary nebula (PPN), and UC. The parameters are selected for multiple reasons. For instance, disk major axes could be used to study the formation theories of giant planets (disk migration and tidal migration). Inclinations affect the surface brightness which contains crucial information of grain properties. System ages are direct manifestations of

Django administration

WELCOME, **ADMIN**. [VIEW SITE](#) / [CHANGE PASSWORD](#) / [LOG OUT](#)

Home > Core > Disks

Select disk to change

[IMPORT](#) [EXPORT](#) [ADD DISK](#)

Action:

0 of 100 selected

<input type="checkbox"/>	OBJECT	CATEGORY	SPECTYPE	RBAND	DISTANCE	DISKMAJORAXIS	INCLINATION	RA	DEC
<input type="checkbox"/>	2MASSI J1628137-243139	TT		17.7	140	4.3	86	16 28 13.70	-24 31 39.0
<input type="checkbox"/>	49 Cet	Debris	A1	5.6	59	9.8	79	01 34 37.78	-15 40 34.9
<input type="checkbox"/>	61 Vir	Debris	G7V	4.2	8.5	22	77	13 18 24.31	-18 18 40.3
<input type="checkbox"/>	99 Her	Debris	F7+K4	4.7	15.6	15.4	50	18 07 01.54	+30 33 43.7
<input type="checkbox"/>	AA Tau	TT	M0	11.8	140	2.3	75	04 34 55.42	+24 28 53.2
<input type="checkbox"/>	AB Aur	HAe	A0e	7.1	144	18	22	04 55 45.93	+30 33 03.6
<input type="checkbox"/>	AS 205 A	TT	K0	12.8	128	0.414	20	16 11 31.36	-18 38 25.3
<input type="checkbox"/>	AS 205 B	TT	K7+M0	14	128	0.19	66	16 11 31.30	-18 38 27.3

Figure 2.1: A screenshot of the database administration. Disk data have been migrated.

old debris disks and young gas disks. Types of the central stars and their masses provide the stage of the stellar evolution. These parameters together produce an outlook of the disk for extensive researches. Sources of disks involve the NASA catalog of circumstellar disks and other published works [27][28].

2.2 Model

Constructing the disk model requires interacting graphic designs. In order to achieve a 3D reconstruction with 2D data, we utilize `three.js`, a cross-browser JavaScript library and application programming interface used to create and display animated 3D computer graphics in a web browser [29]. The disk is created with the `three.js` primitive module `LatheGeometry`. Given the 2D silhouette as a series of points with a certain amount of subdivisions, the module generates the shape by spinning the silhouette around an axis. Vertex positions of the outline are determined by disk height profiles. The model implements the disk of the Herbig Ae/Be star HD 97048, whose scattering surface height H at a separation r from the star can be described reasonably well with a single power law of the form

$$H(r) = 0.0064 \text{au} \cdot \left(\frac{r}{1 \text{au}}\right)^{1.73}, \quad (2.1)$$

up to a separation of ~ 270 au [3]. [Figure 2.2](#) shows the side view of the disk structure. The upper and lower part of the closed shape makes use of the measured height profile. We rotate the disk skeleton around the z-axis of the origin, which is set at 3 units away from the left end, and the model is therefore constructed. Due to GPU limitations, the

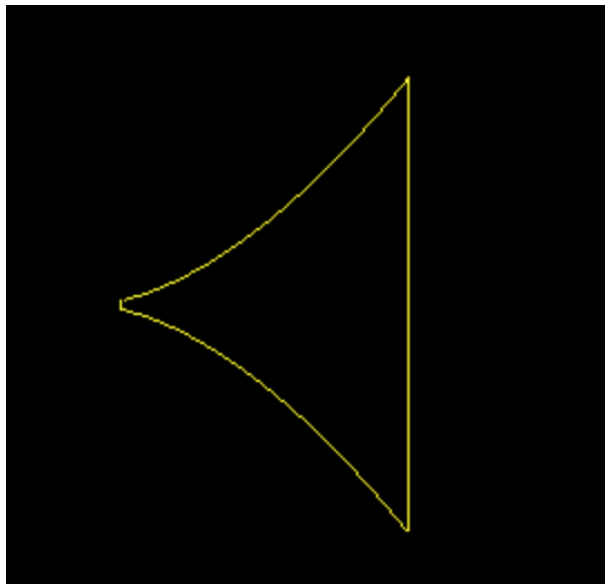


Figure 2.2: The cross-section of the disk skeleton. The upper and lower curves are determined by [Equation 2.1](#). The edge of the inner disk cuts off before the origin so that the disk does not reach the central star.

separation is scaled down to 1/10 of the original value and the coefficient is multiplied by 10 for consistency. Furthermore, HD 97048 has an inclination of 39.9 ± 1.8 degrees [3]. An inclined disk is simulated by the initial camera position. In this case, the coordinate of the camera is set to be $(0, 60, 60 * \tan(39.9))$, fitted to the size of the window.

`Three.js` sets the default color of any created object to white. Nonetheless, in reality, colors of observed circumstellar disks are governed by the polarized intensity phase function, which is the total intensity of the disk affected by the scattering polarization. With the polarized intensity calculated, the phase function can be used to set the color intensity of the disk. Each specific value of the phase function determines all three color components (RGB) to a scalar with a value between 0.0 and 1.0. This setup generates a dark grey for strong scattering and a light grey for weak scattering. We will discuss the reasons for the disk choice, as well as the scientific aspects in detail in [Chapter 3](#).

Chapter 3

Discussion

We choose HD 97048 as the starting point of this model construction for multiple reasons. First of all, it is one of few young gaseous disks (~ 2 Myr) with a measured height profile and exact scattering angles. Typically old debris disks (~ 10 Myr) are difficult to obtain these quantities with sufficient precision. Part of the reasons is that few works have focused on the subject. More importantly, detailed measurements demand disk structures to fit the observation, yet the rings in old disks usually are not clear, making researchers incapable of tracing the eclipses. Often the disk offsets are too close to the front side and too far from the backside. On the contrary, young disks allow for measuring phase functions from disk structures. Among them, HD 97048 is considered a special one. The central star is roughly $2M_{\odot}$, relatively massive as a host. More massive stars provide more dust for the disk to grow and extend to a larger separation. Therefore, HD 97048 is a valid foundation to build up the disk reconstruction.

3.1 Scattered light phase function

The scattered light phase function is the angular distribution of light intensity scattered by a particle at a given wavelength, determined by the scattering angle ϕ with respect to the incident beam. The phase function refers to the intensity (radiance) at ϕ relative to the normalized integral of the scattered intensity at all angles, defined as

$$P(\phi) = \frac{F(\phi)}{\int_0^{\pi} F(\phi) \sin \phi d\phi}, \quad (3.1)$$

where $F(\phi)$ is the intensity (radiance) [30]. $P(\phi)$ is regarded as a probability density function, indicating the chances of a photon being scattered in a particular direction of ϕ . The surface brightness of a circumstellar disk brings insight to the disk evolutionary process. For an inclined disk, the surface brightness is governed by the scattering phase function of the dust which depends on grain properties such as size, shape, structure, and index of refraction [31]. Since the light scattered by dust grains in the disk is polarized, measurements of the phase function of the scattered light with polarization will allow for modeling the disk structures more precisely to high-resolution observations. Therefore, we implement and examine several different phase functions to understand the disk behavior at various scattering angles.

Traditional method to describe the scattering phase function of disks is by the Henyey-

Greenstein (HG) function, with an expression of

$$HG(g, \phi) = \frac{1}{4\pi} \frac{1 - g^2}{(1 - 2g \cos \phi + g^2)^{3/2}}, \quad (3.2)$$

where g is an anisotropy factor and ϕ is the scattering angle [32]. The parameter g

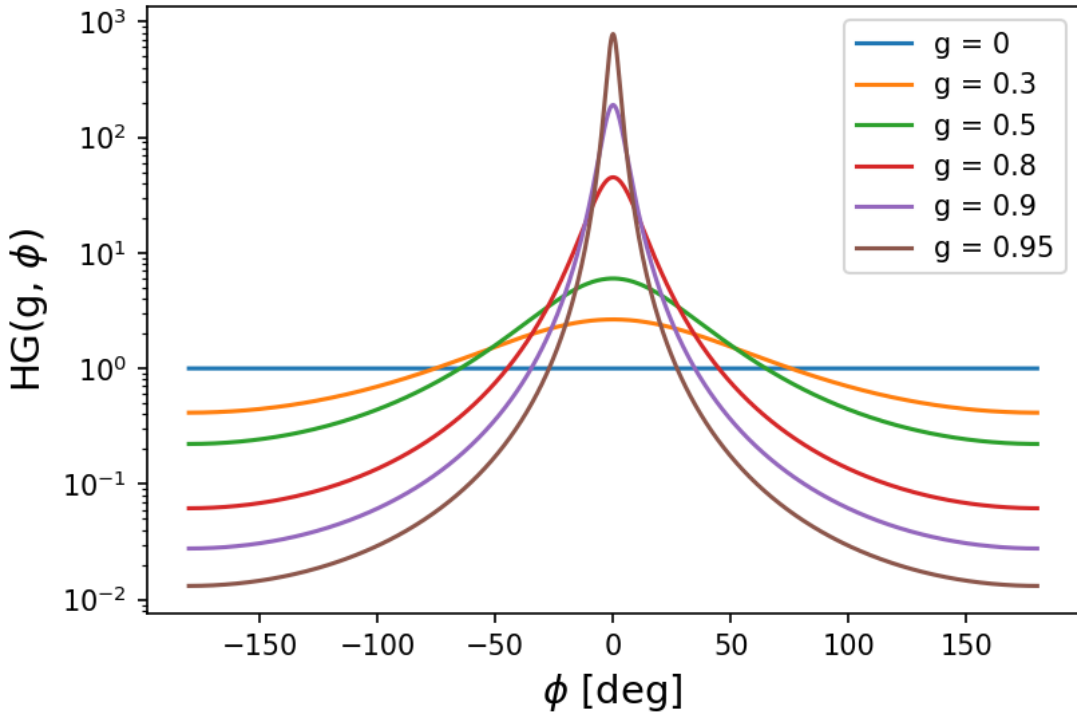


Figure 3.1: The HG functions at different anisotropic levels. The scattered light is distributed less evenly as the g value increases.

ranges from -1 for perfectly backward scattering to 1 for perfectly forward scattering, with 0 corresponding to isotropic scattering. Figure 3.1 and Figure 3.2 show the HG functions with different anisotropic parameters. The increasing g value leads to more uneven distributions of surface light. It specifies the HG function such that the expectation value of $\cos(\phi)$ returns identical g , resulting in an identity function. However, considering that the HG function is monotonic, matching it with scattering phase functions having multiple peaks can be problematic. Previous studies have shown that a linear combination of multiple HG functions yield satisfactory quick approximations to the measured SPF in planetary rings or dusty debris disks [33][34]. An attempt to attain a sufficient approximation is fitting the scattering phase function with a two-component HG function of the form

$$HG_2(g_1, w_1, g_2, w_2, \phi) = w_1 HG(g_1, \phi) + w_2 HG(g_2, \phi), \quad (3.3)$$

where $g_1 = 0.99^{+0.01}_{-0.38}$ and $g_2 = -0.14 \pm 0.006$ are the two HG parameters and $w_1 = 4.0$ and $w_2 = 0.82$ are the coefficients for the forward and backward scattering, respectively [1]. These parameters are generated base on the measurement of HR 4796 A, an old debris-rich disk observed in scattered light as an inclined ring with a high surface brightness.

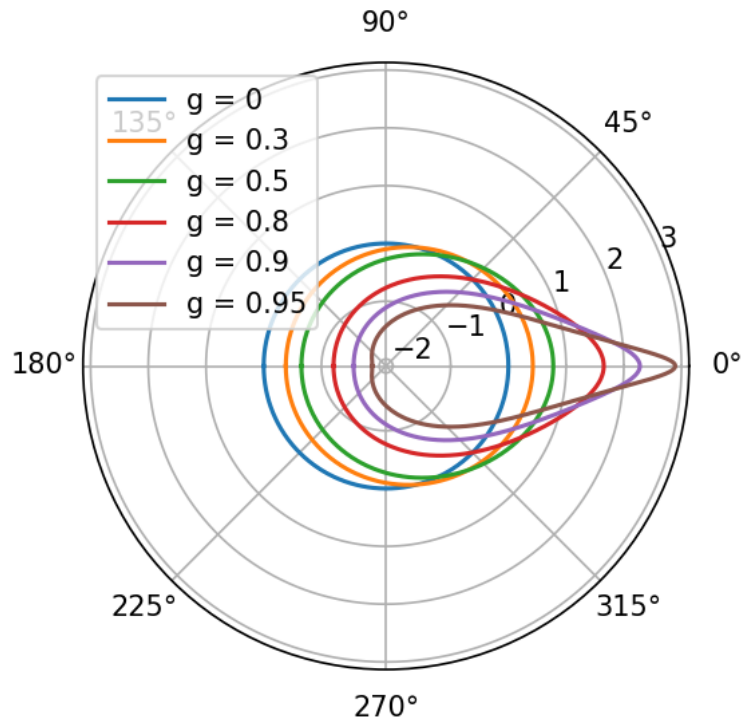


Figure 3.2: Figure 3.1 in the polar coordinate.

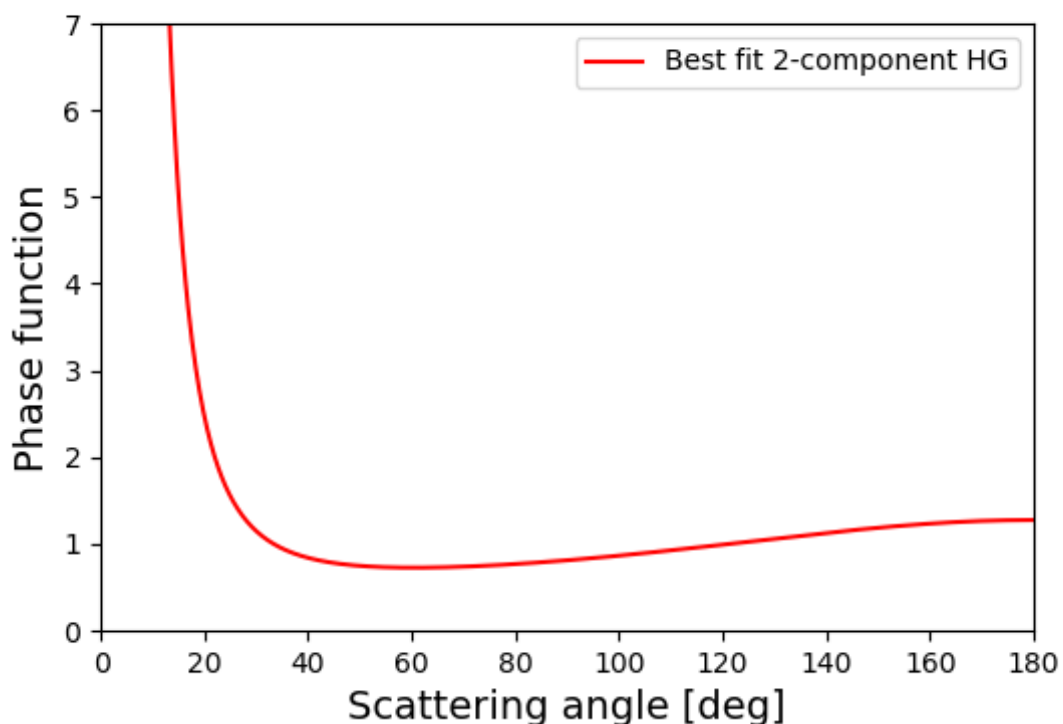


Figure 3.3: Fit of the scattering phase function with a two-component HG function, with two asymmetric parameters $g_1 = 0.99^{+0.01}_{-0.38}$ and $g_2 = -0.14 \pm 0.006$, and two coefficients $w_1 = 4.0$ and $w_2 = 0.82$. This figure is reproduced with VLT/SPHERE data [1].

[Figure 3.3](#) shows the calculated phase function versus scattering angle. Note that the linear mapped HG function only returns the total intensity.

The scattering angle is computed by the Euclidean dot product of the camera direction, a 3D vector representing the world space direction in which the camera is looking, and the face centroid, a vector connecting the origin with the center of each facet of the disk. [Figure 3.4](#) provides an illustration of the computation. The triangle refers to a

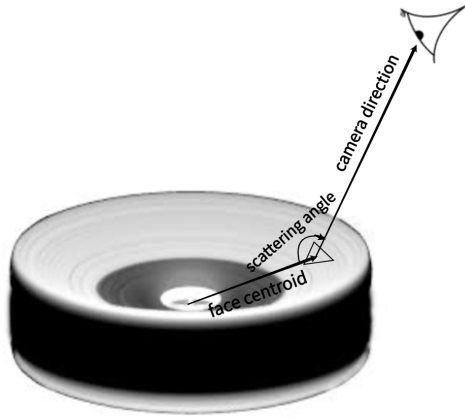


Figure 3.4: Model illustration of the scattering angle computed from the face centroid vector and camera direction vector of each facet.

particular facet on the surface of the disk. For every single facet, there is a corresponding vector from the central star and a vector pointing to the camera. The dot product of the two quantities yields a cosine function. The inverse trigonometry then produces the scattering angle for this facet. We loop over the entire disk to calculate all scattering angles. The disk is positioned at the origin, yet the camera is set to move freely by the `OrbitControls` module of three.js. As the camera rotates, the vector describing the camera direction changes, resulting in a variation of the scattering angle.

Polarization imaging observations measure polarized intensity, and thus the total intensity phase function needs to be corrected. The polarized intensity phase function is affected by both the total intensity phase function and the degree of polarization. For single scattering light, the degree of polarization is yielded by the single scattering polarization. Therefore, we apply the Rayleigh single scattering polarization,

$$P = -\frac{\cos^2 \phi - 1}{\cos^2 \phi - 1}, \quad (3.4)$$

where ϕ refers to the scattering angle [35]. [Figure 3.5](#) shows a visual illustration of the scattering disk, along with a typical bell-shaped degree of polarization. The polarized intensity phase function is estimated by multiplying the total intensity phase function with the single scattering polarization, which can be regarded as the polarization efficiency in this case. As a result, the polarized intensity can be reconstructed to compare with the observation data.

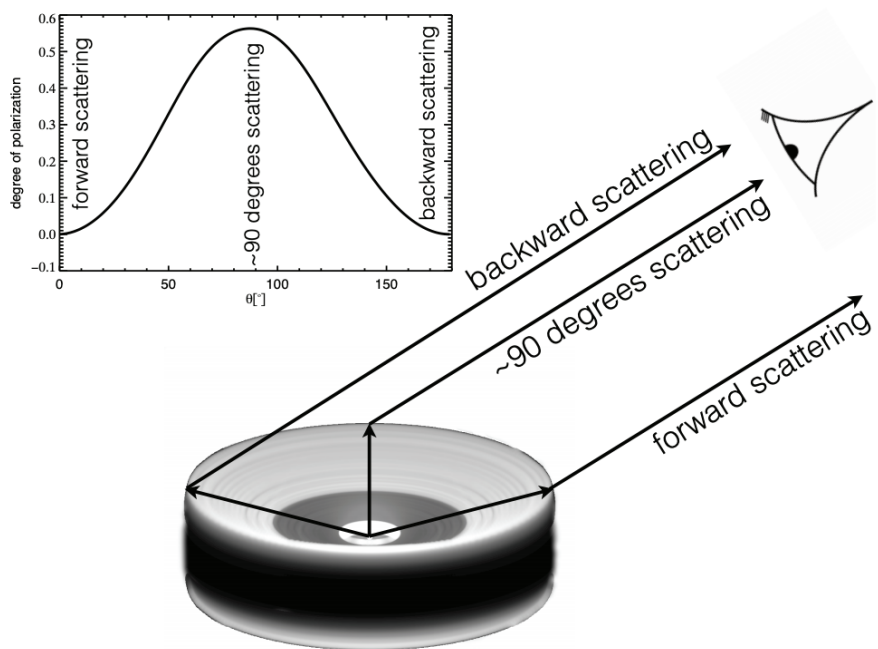


Figure 3.5: Model illustration of the scattering angle in domination depending on observations from different regions of the disk. The inset shows the typical shape of a polarization phase curve. Together the two images reveal the relation between the expected degree of linear polarization and the location in the disk. This figure is duplicated for clarification [2].

3.2 Fitting of disk features

The observed total intensity is fitted numerically to reproduce on the disk model. Three methods have been applied to task: a two-component HG function, a three-component HG function, and high-order polynomials. We include polynomials fitting for various reasons. Technically, astronomical studies require curve fittings capable of producing scientific interpretations, which means that each one of the coefficients and parameters must refer to physical phenomena. Nevertheless, in this work, we aim to inspect the similarities and differences between the observed and modeled disks by visualization. The focus is not to investigate the physics behind the measurements, but to reproduce the disks in three-dimensional graphics with two-dimensional data. Therefore, the priority in the fittings is to generate curves as close as to the measure phase functions, whereas explanations of the constants and worries about possible overfitting become less important. In practice, the curve fitting makes use of the array-processing library `Numpy` (version 1.18.1) and the scientific computing library `Scipy` (version 1.4.1) in Python [36][37]. We analyze each method individually and compare them with the actual data.

3.2.1 HD 97048

An observation of HD 97048 in polarized and integrated light has been carried out using the InfraRed Dual-band Imager and Spectrograph (IRDIS), the near-infrared subsystem of VLT/SPHERE [3][38][25]. Figure 3.6 shows the polarized intensity phase functions

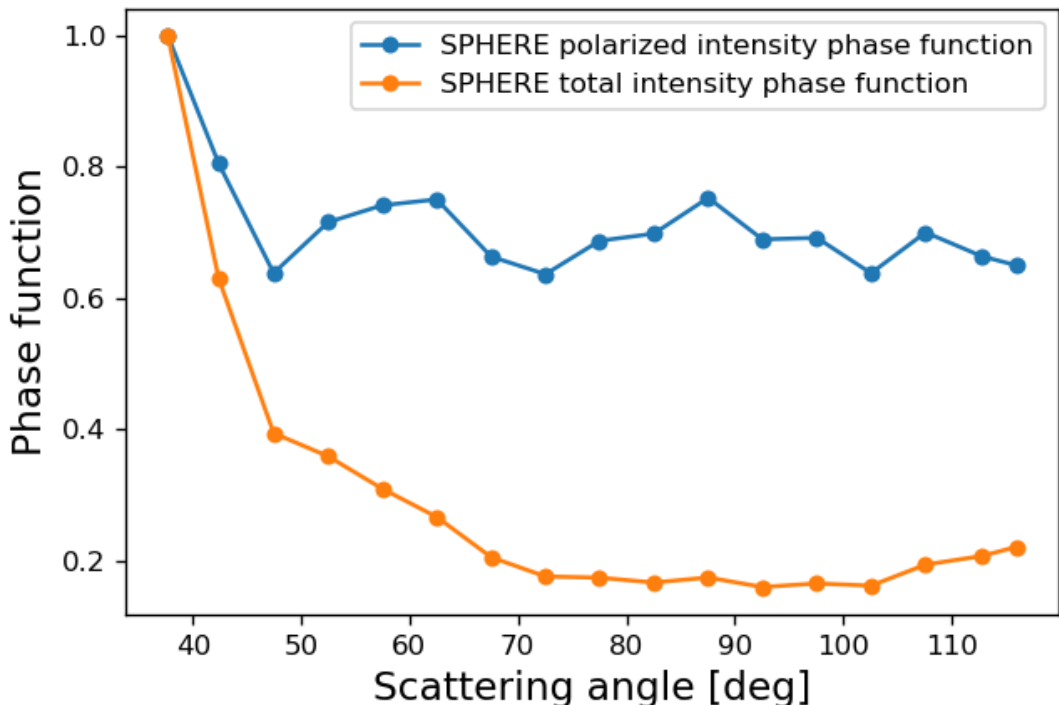


Figure 3.6: Polarized and total intensity phase function obtained from the SPHERE data. Both phase functions have been normalized to their peak value. The uncertainties have been omitted for clarity. This figure is reproduced with VLT/SPHERE data [3].

acquired from the SPHERE data, along with the total intensity phase function estimated from the ratio of the polarized intensity phase function and the degree of polarization. All data points have been normalized with respect to their peak values and the error bars have been omitted for clarity. As shown, The scattering angle ranges from approximately 37.7 to 116.0 degrees, as the smallest angle probed only reaches 35 degrees. For most scattering angles, the polarized intensity phase function reveals a roughly isotropic behavior; the dust density distribution is nearly uniform azimuthally and the dust properties are close to identical azimuthally. On the other hand, the trend shows a weak forward scattering, indicating that the near side of the disk is brighter than the far side in total intensity. Ideally, if the disk is implemented with the correct phase function, the visual effect should return similarities.

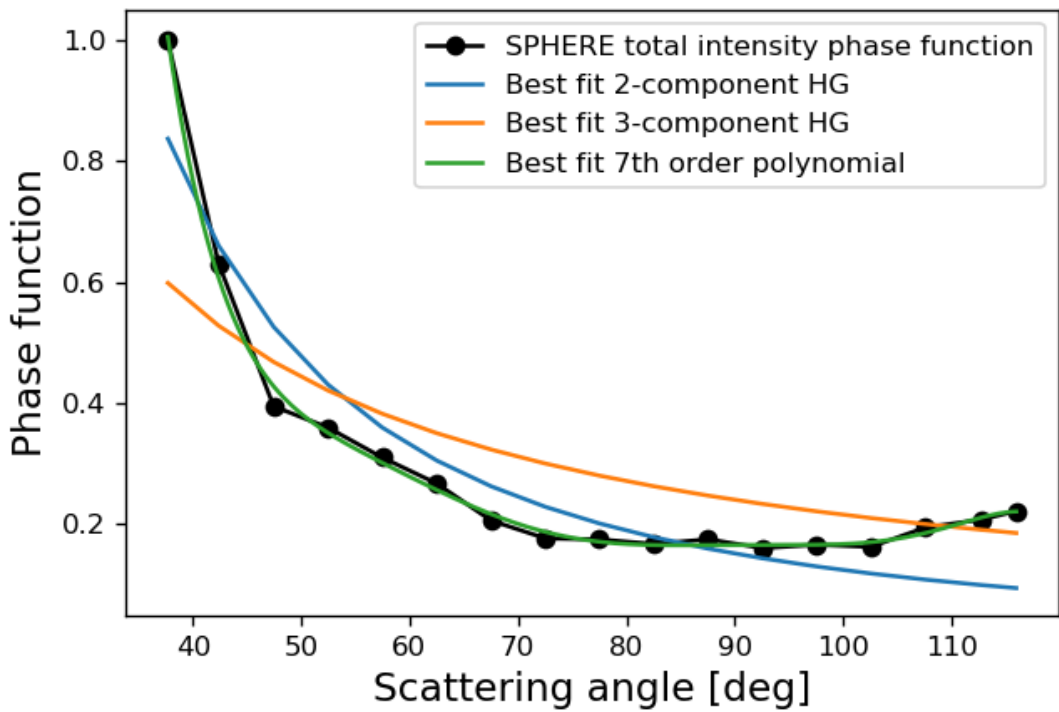


Figure 3.7: The SPHERE total intensity phase functions fitted with various methods. A 7th order polynomial yields the best fit curve compared to both two and three-component HG functions.

As shown in Figure 3.7, the three methods are plotted together with the observed SPHERE total intensity phase function with respect to scattering angles. The two-component HG function fits poorly while the three-component HG function seems only slightly more plausible. Originally we intend to fit the curve solely using the two-component HG function, yet we decide to attempt different approaches with the deficient result coming out. In fact, the two-component HG function even performs better in the curve fitting, as the parameters are calculated unambiguously. The three-component HG function fit could never be optimized because the covariance of the parameters could not be estimated. In order to obtain a tractable result, the computation is conducted with a brute force restriction. Since the total intensity appears with a strong forward scattering and a weaker backward scattering in the observed range, the first two g parameters are

set to be positive and negative, respectively, with the last one set to an absolute value of 0.5 from 0. Previous studies imply that the lack of a backward scattering feature in the measured total intensity is not expected to impact the best-derived fit [34][39]. It is evident that both the two and three-component HG functions fit inadequately to the total intensity of HD 97048.

Another approach to acquire a numerical solution of the phase functions is to fit the data points with high-degree polynomials, which provide an adequate approximation of the non-linear relationship between the independent and dependent variables. Since most phase functions are composed of wide range curvatures, polynomial fits become advantageous because of their flexibility and capability to describe models that must be developed empirically.

The best fit curve is achieved by a 7th degree polynomial. The coefficients are listed in

HD 97048	
order	coefs
0	96.50
1	-8.968
2	0.355
3	-7.675×10^{-3}
4	9.811×10^{-5}
5	-7.402×10^{-7}
6	3.053×10^{-9}
7	-5.314×10^{-12}

Table 3.1: Orders and corresponding coefficients of the polynomial fit to the SPHERE total intensity phase function.

Table 3.1. This function portrays the steep forward scattering regime and the flat region from around 70 to 100 degrees quite accurately. As previously mentioned, the data fitting does not concentrate on interpreting the real physics of the surface brightness, but on replicating the measured phase function. We seek for the best fit curve that allows us to reconstruct the disk resembling the observation. Hence, we collect the optimized parameters and neglect their physical meanings.

3.2.2 Porous dust aggregate model

In addition to the VLT/SPHERE observation of HD 97048, radiative transfer simulations have been performed to study scattered light properties of circumstellar disks at near-infrared (NIR) wavelengths for various dust size and structure [4]. Here we implement the porous dust aggregate model, which contains two types of fractal dust aggregates, ballistic cluster cluster agglomerate (BCCA) and ballistic particle cluster agglomerate (BPCA), shown in [Figure 3.8](#).

[Figure 3.9](#) shows the optical properties produced by the BCCA and BPCA models. These two simulations are carried out using the T-Matrix and Quasi-Monte Carlo orientation averaging method [40][41]. Scattering appears to anisotropic for BCCA and BPCA because these aggregates have the radii larger than $\lambda/(2\pi)$, where λ represents the NIR wavelength of interest [4]. For these two porous dust aggregate models, the disk shows asymmetry in total intensity (brightness intensity in disk visualization), due to strong forward scattering and high polarization.

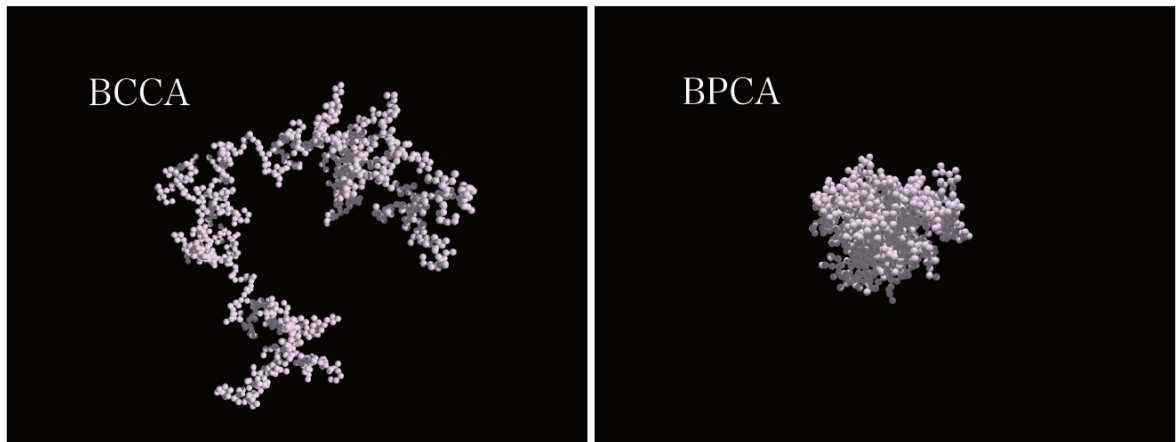


Figure 3.8: Morphology of porous dust aggregates. Left and right panels correspond to the BCCA and BPCA models, respectively. This figure is duplicated for clarity [4].

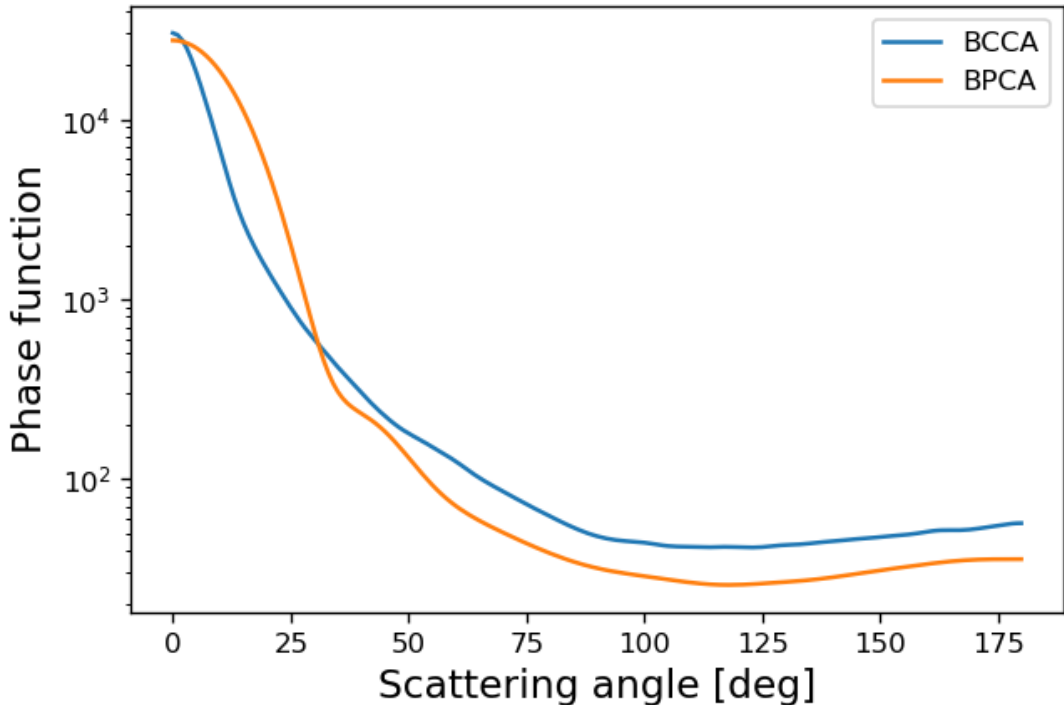


Figure 3.9: Optical properties of the BCCA and BPCA models in log scale. This figure is reproduced with the data obtained from simulations using the T-Matrix and Quasi-Monte Carlo orientation averaging method [4].

The fitting process of BCCA and BPCA models is generally similar compared to that of data obtained from direction observation. The fitting with two and three-component HG function turns out to be implausible for BCCA model. The initial trial with no restrictions yields unconverged results, as the optimization procedure fails to complete within the computing limit. A few attempts of brute force bounds are sufficient to produce a finite solution, yet the two fitted curves appear to be significantly deviated from the data points, as manifested by [Figure 3.10](#). The three-component fitted phase function decreases less than the two-component fitted phase function. This is likely due to the uncertainty caused by the extra two parameters. In the meantime, the best fit curve is

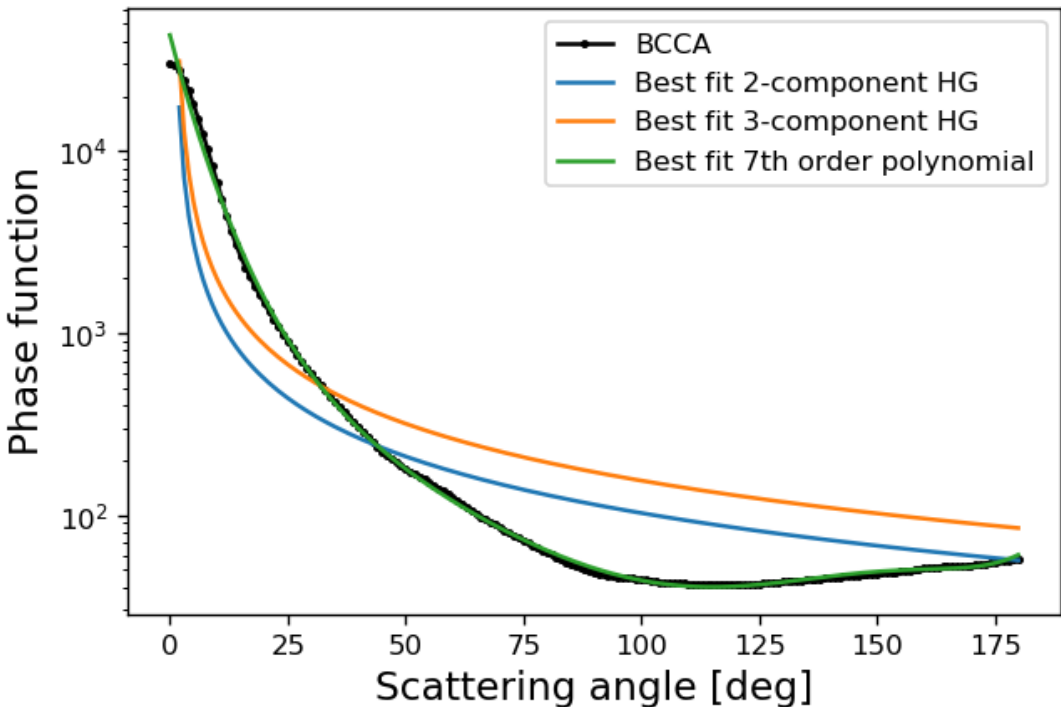


Figure 3.10: The BCCA phase functions fitted with various methods. A 7th order polynomial yields the best fit curve compared to both two and three-component HG functions. The y-axis is log-scaled.

again provided by a 7th degree polynomial. The goodness of this fit indicates that the high-order polynomial fitting is overall suited to the model data, except that the head of the curve is slightly off the target, probably caused by the extremely high total intensity at 0 scattering angle. [Table 3.2](#) lists all coefficients with their correspondent order.

The overall shape of BPCA model shares numerous common similarities with that of the BCCA model and two phase functions are nearly the same in order of magnitudes. As in all previous figures, a 7th order polynomial fit is plotted together with a two and a three-component HG function, shown in [Figure 3.11](#). It is obvious that HG function fittings are not optimal even with brute restrictions. The 7th degree polynomial produces the best curve fit. The coefficients and correspondent orders are listed in [Table 3.3](#).

BCCA	
order	coefs
0	4.637
1	-0.099
2	0.002
3	-9.850×10^{-6}
4	-6.887×10^{-8}
5	1.477×10^{-9}
6	-8.181×10^{-12}
7	1.529×10^{-14}

Table 3.2: Orders and corresponding coefficients of the polynomial fit to the BCCA total intensity phase function.

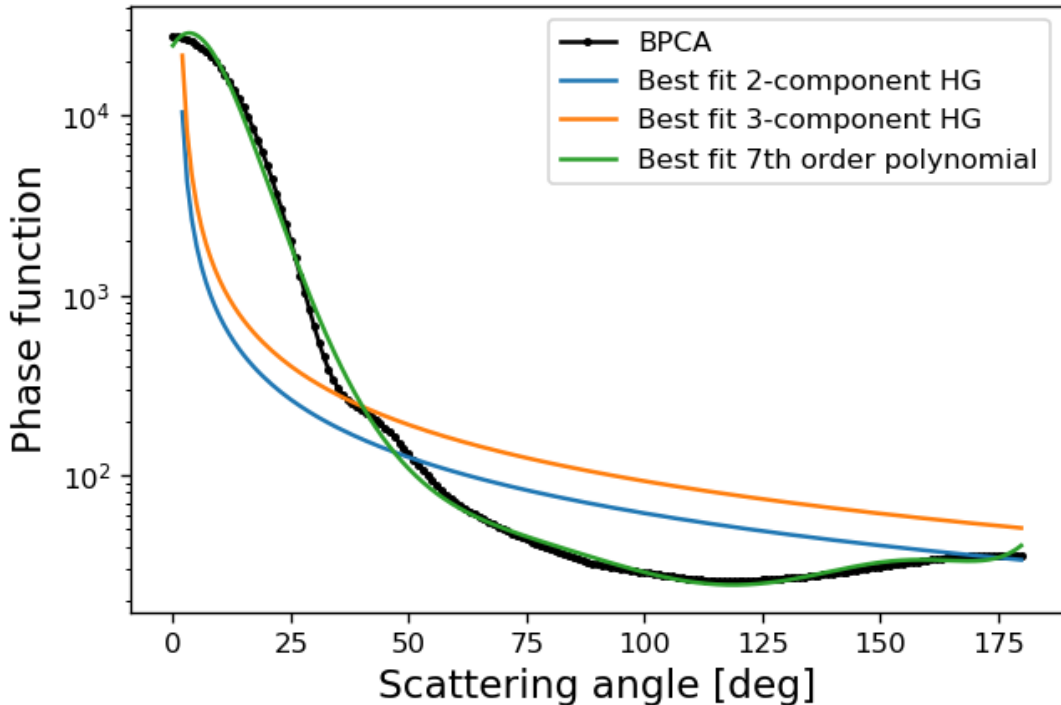


Figure 3.11: The BPCA phase functions fitted with various methods. A 7th order polynomial yields the best fit curve compared to both two and three-component HG functions. The y-axis is log-scaled.

BPCA	
order	coefs
0	4.388
1	0.042
2	-0.007
3	1.990×10^{-4}
4	-2.651×10^{-6}
5	1.872×10^{-8}
6	-6.745×10^{-11}
7	9.756×10^{-14}

Table 3.3: Orders and corresponding coefficients of the polynomial fit to the BPCA total intensity phase function.

3.3 Comparing observations with models

High-order polynomial fittings provide mathematical expressions that can be used to illuminate the disk model. We compare two observational results (measured phase function of HR 4796 A and HD 97048) and two computational models (BCCA and BPCA of the porous dust aggregate model) with our disk model. Each model is shaded by the corresponding fitting function and visualized. The phase functions are plotted for detailed analysis.

3.3.1 HD 97048

The first comparison of the measured image to the disk model is shown in Figure 3.12, where the model is described by a two-component HG function parametrized by the measured phase function of HR 4796 A [1]. HD 97048 reveals a stronger forward scattering than the backward scattering. Because the disk is inclined by 39.9 degrees, the SPHERE DPI Q_Φ image shows an elliptical shape. As we can see from the model, after the disk is tilted for the same degree, the disk displays a similar shape and overall pattern. The central star is not included as we assume a perfect coronograph. A dark color on the right side implies a strong forward scattering, but no direct evidence is observed. Nonetheless, the backward scattering appears to be more intensive compared to the observed image. This phenomenon can also be interpreted from the phase function.

The total intensity phase function remains at a relatively high value, where the local minimum is at approximately 0.3. The range of the scattering angle in this plot is between 20 and 160 degrees. In theory, the scattering angle ranges from 0 to 180 degrees. In practice, however, the observed data of HR 4796 A only range from 13.6 to 166.6 degrees. Moreover, we find that in our model the angles less than roughly 20 degrees correspond to extreme values in the phase function, which outshine any other polarization and disk pattern. Hence, we replace all of these angles with degrees of 20 and normalize the phase function to these values. The scattering angle is cut at the end of the observed data points. The bell-shape degree of polarization successfully reflects the applied Rayleigh scattering.

The second disk model to compare is described by the previously mentioned high-order polynomial fit of the SPHERE/VLT observational result [3]. Shown in the top right of Figure 3.13, a grey color dominates most of the disk model, indicative of a overall

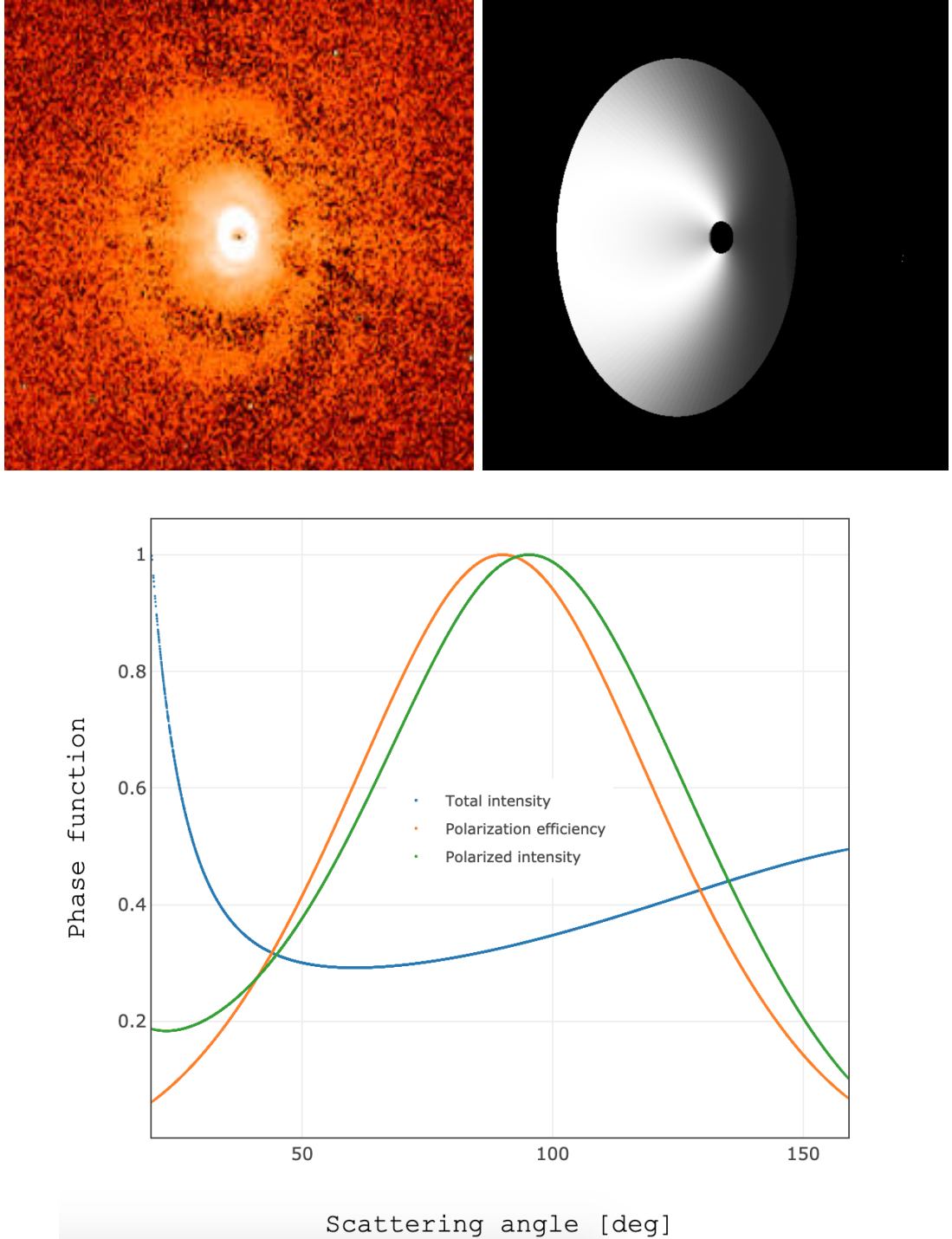


Figure 3.12: *Left:* reduced SPHERE DPI Q_Φ (the azimuthal counterparts of the Stoke vectors Q) image of HD 97048 [3]. *Right:* the disk model reconstructed with a power-law height profile measured from HD 97048 and a color scalar set by the polarized intensity computed with observational data of HR 4796 A. The star is not included for perfect coronagraphy. *Bottom:* the total intensity phase function (blue curve) and the computed polarized intensity phase function (green curve) obtained from multiplying with the polarization efficiency (orange curve). The model is described by a two-component Henyey-Greenstein function, parametrized by the two HG parameters, $g_1 = 0.99^{+0.01}_{-0.38}$, $g_2 = -0.14 \pm 0.006$, and the coefficients $w_1 = 4.0$ and $w_2 = 0.82$ [1]. The phase functions have been normalized to their values corresponding to the 20-degree scattering angle.

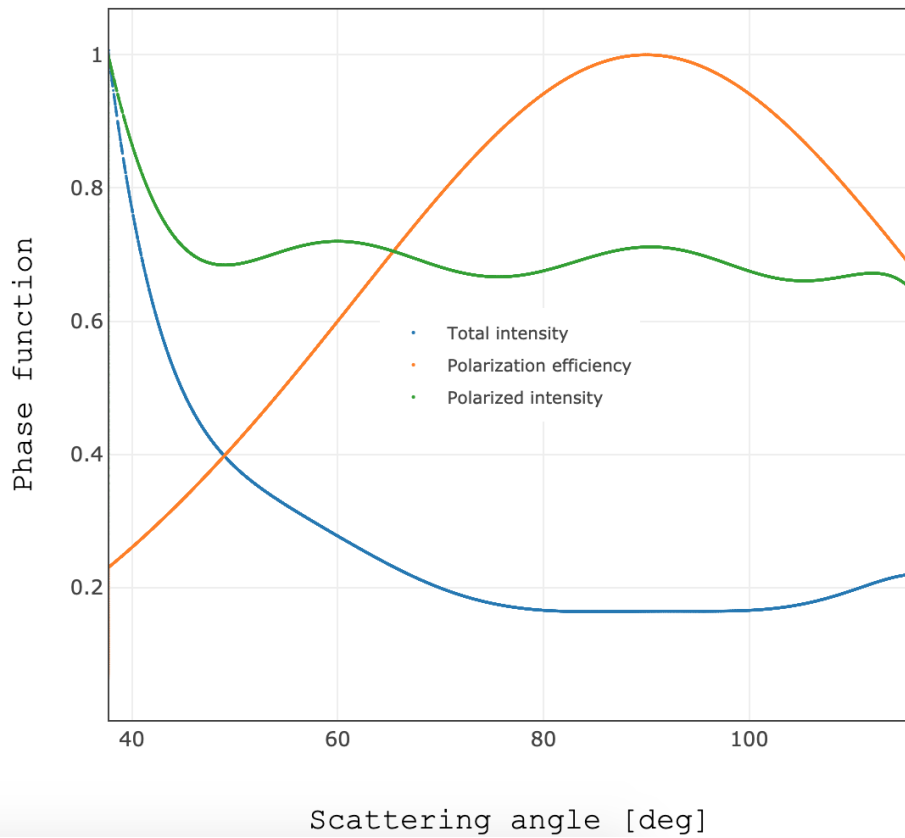
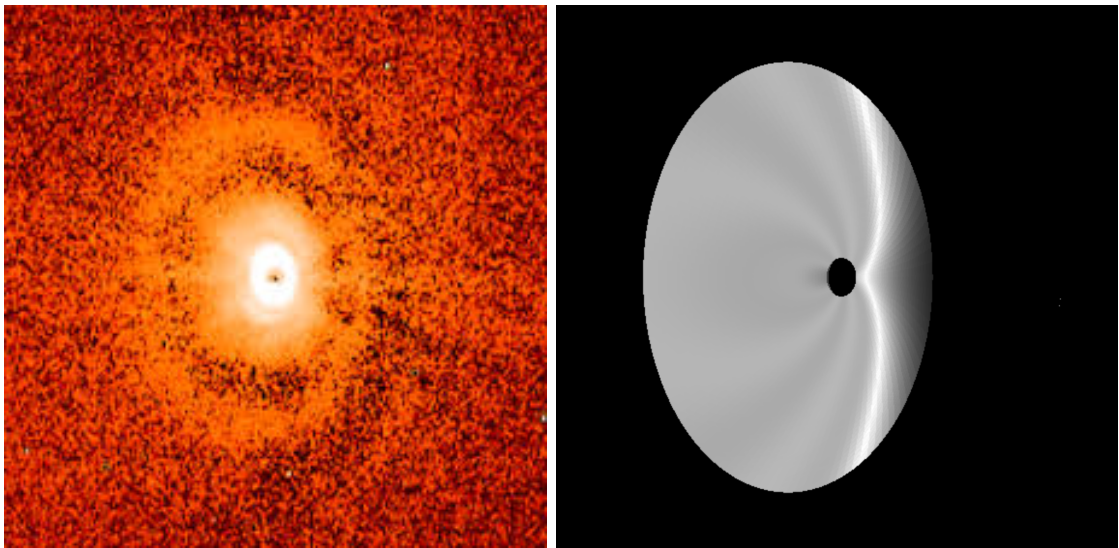


Figure 3.13: *Left:* same as in Figure 3.12. *Right:* the disk model reconstructed with a power-law height profile measured from HD 97048 and a color scalar set by the polarized intensity computed with observational data of the same disk. The star is not included for perfect coronagraphy. *Bottom:* same as in Figure 3.12, except that the phase functions are calculated using a 7th order polynomial fitted to the observation data of HD97048 [3]. The phase functions have been normalized to their peak value.

stronger scattering compared to the model profiled by the two-component HG function. The forward scattering is clearly revealed by the white region on the right of the disk model. The shape of the total intensity matches well with the phase function measured from SPHERE Q_Φ , as well as that of the reconstructed polarized intensity function. The measured scattering angle vary between 37.7 and 116.0 degrees. Within the range no extreme value of the intensity impairs the overall pattern. Therefore, we normalize the phase functions to their peak value.

Following the two observation-model comparisons are two model-model comparisons involving the porous dust aggregate model [4]. Both BCCA and BPCA models show relatively strong scattering and moderate backward scattering in the phase function. The scattering angle in models extends further, from 0 to 180 degrees, since there exist no probing limits as in observations. The lack of extreme values allows for normalizing the phase functions once again to their peak value. Unfortunately, the effect of strong forward scattering on the disk could not be seen easily from visual inspection.

Although the two models are barely distinguishable to the model described by the HR 4796 A parametrized two-component HG function, the phase functions still show evident weaker forward and backward scattering. We see from [Figure 3.14](#) and [Figure 3.15](#) that the total intensity curves of both BCCA and BPCA model are relatively flatter compared to [Figure 3.12](#). The normalized total intensity phase functions drop from 1 to approximately 0.35 at around 110 degrees, whereas in the first comparison the local minimum (also ~ 0.35) locates at around 60 degrees; the steepness of BCCA and BPCA phase functions is smaller than that of the model portrayed by measured phase function of HR 4796 A. Similar patterns are observed from the SPHERE measured phase function of HD 97048, where the local minimum of the total intensity locates at around 90 degrees. Moreover, the difference between the local maximum and local minimum is approximately 0.85, significantly bigger than the other phase functions.

One thing to pay attention to is the shape of the polarized intensity phase functions. Reconstructed from multiplying the total intensity phase functions with the bell-shape degrees of polarization, polarized intensity phase functions all present similar shapes, except the SPHERE measured data of HD 97048, where the shape is generally flat compared to the others. This is likely due to the different ranges of data. The two observed phase functions are restricted by the probing limit of telescopes and thus the scattering angle only resides partially of the entire hemisphere, while the two modeled phase functions indeed cover all 180 degrees of scattering angles. Within each subgroup, the measured phase function of HR 4796 A ranges from 20 to 166.6 degrees, whereas that of HD 97048 only spans the angles between 37.7 and 116.0 degrees. The two modeled phase functions using the porous dust aggregate model display no obvious differences in phase functions and disk models. Notice that the gap between the inner and the outer ring in the SPHERE image is not observed from the model. We have not coded this part until the completion of this writing. Future works shall add more details of the disk.

3.3.2 Other disks

In order to further test the model performance in reconstruction, we would like to examine several more disks. The idea is to see whether they share any common similarities in evolutionary processes, dust properties, or disk profiles. [Table 3.4](#) lists four disks that are specifically chosen based on their sizes and inclinations. The models are ordered from low to high inclination. In theory, the scattering effect will become gradually clear as the

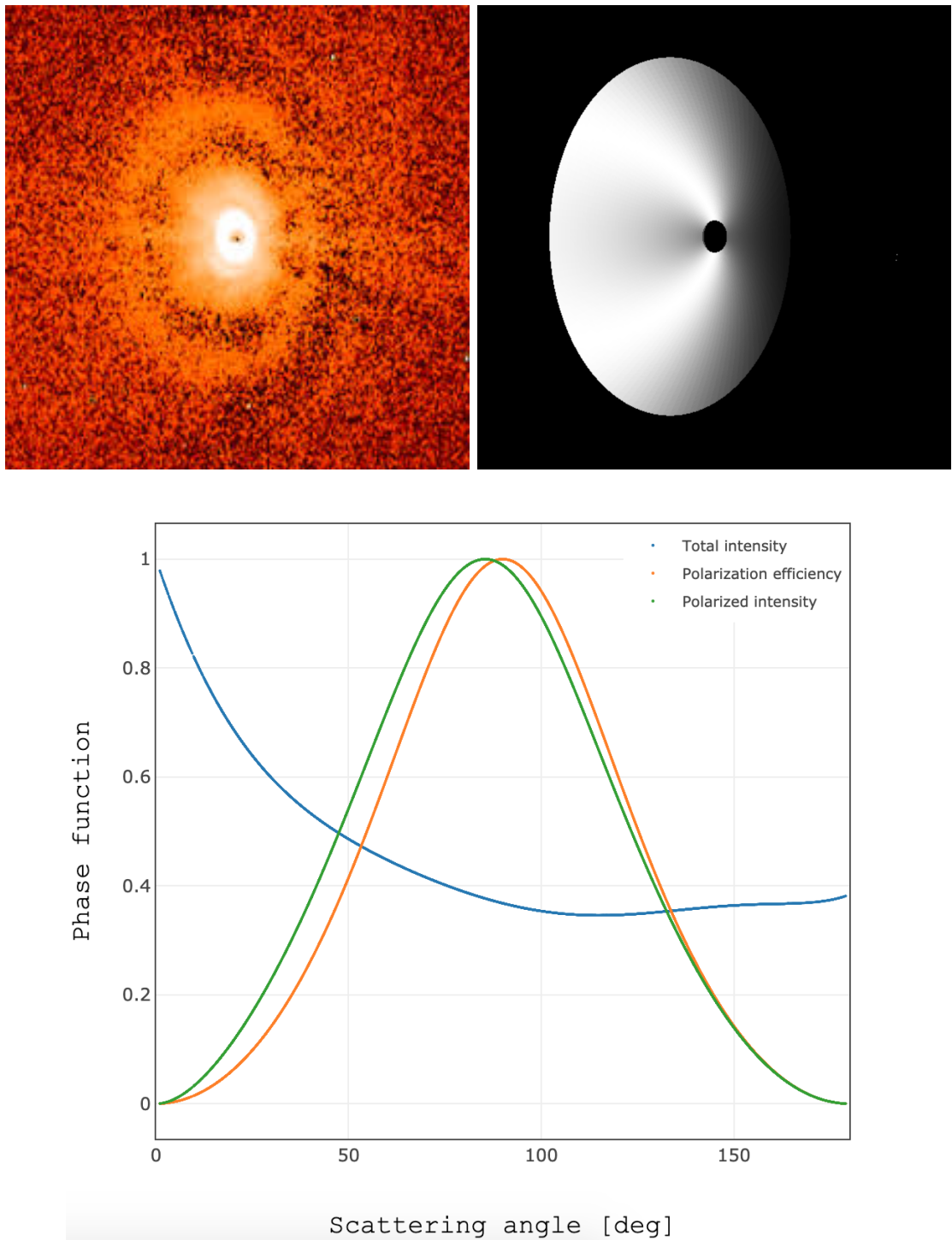


Figure 3.14: *Left:* same as in Figure 3.12. *Right:* the disk model reconstructed with a power-law height profile measured from HD 97048 and a color scalar set by the polarized intensity computed with the porous dust aggregate model. The star is not included for perfect coronagraphy. *Bottom:* same as in Figure 3.12, except that the model is described by a 7th order polynomial fitted to the BCCA type of fractal dust aggregates of the porous dust aggregate model [4]. The phase functions have been normalized to their peak value.

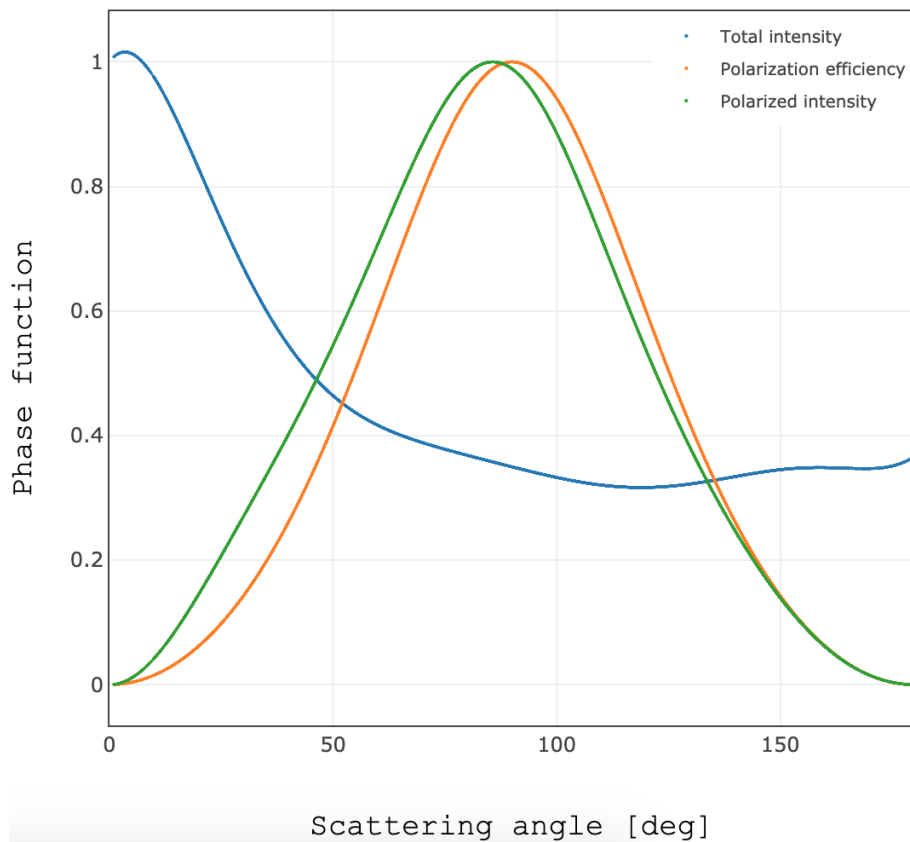
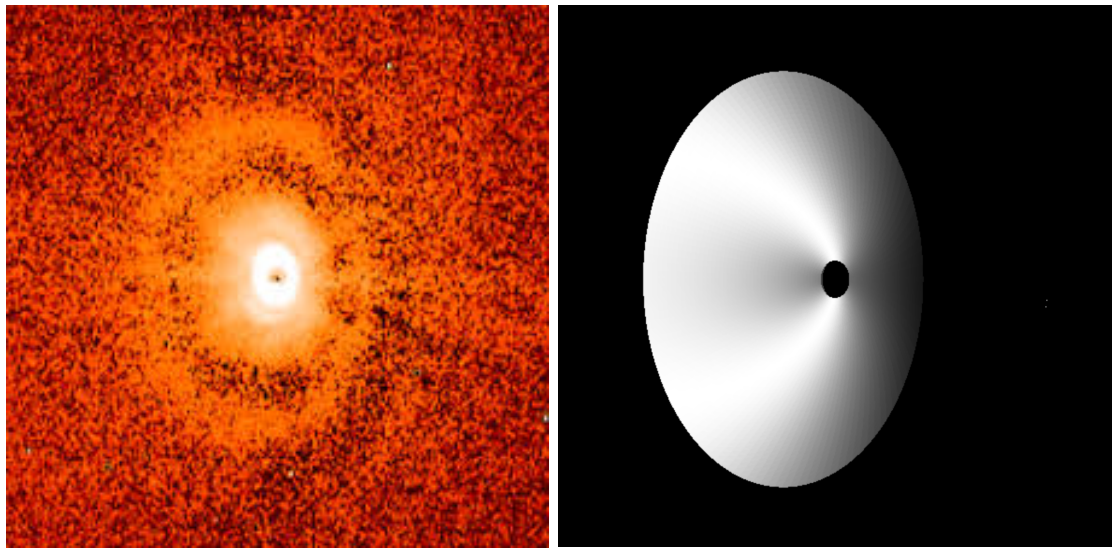


Figure 3.15: *Left:* same as in Figure 3.12. *Right:* the disk model reconstructed with a power-law height profile measured from HD 97048 and a color scalar set by the polarized intensity computed with the porous dust aggregate model. The star is not included for perfect coronagraphy. *Bottom:* same as in Figure 3.12, except that the model is described by a 7th order polynomial fitted to the BPCA type of fractal dust aggregates of the porous dust aggregate model [4]. The phase functions have been normalized to their peak value.

Disk List			
Name	Inclination	Position angle	Age
HD 169142	13	5	6^{+6}_{-3}
PDS 66	30.26	189.19	17 ± 5
IM lup	55	325	1.1 ± 0.2
MY lup	77	239	12.7 ± 4.4

Table 3.4: Disks chosen to implement with different phase functions and to compare with the observational results. Detailed properties of each disk are obtained from various literature [5][6][7].

inclined angle increases.

In theory, the scatterings are stronger for highly inclined disks. [Figure 3.16](#) shows that, with a 13-degree inclination, HD 169142 displays only a small-scale scattering due to its low inclination. As the inclination increases, we can see from [Figure 3.17](#) that the PDS 66 inclined by 30.26 degrees reveals a more obvious forward scattering. At large inclination angles, disks such as IM lup (55-degree inclination) and MY lup (77-degree inclination) manifest strong scattering effects, as shown by the high color contrasts in [Figure 3.18](#) and [Figure 3.19](#).

An interesting phenomenon is that the offset of centers grows stronger with larger extensions of disk models. For instance, PDS 66 models show a weaker offset compared to those of HD 97047. A stronger offset indicates stronger disk flaring; PDS 66 models show less flaring than the HD 97048 models. One possible explanation is that PDS 66 has a smaller height profile (100.0 AU vs ~ 270 AU). As shown in [Equation 2.1](#), we apply a power-law height profile to describe the disk structure. If the size of the disk is considerably smaller than HD 97048, its cross-section will look like a flat surface and the disk flaring will indeed be notably weaker. In contrast, models of IM lup show significantly stronger flaring, due to their immense sizes compared to those of HD 97047 (452.2 AU vs ~ 270 AU). HD 169142 models are observed with only an obscure offset because of its low inclination; the disk surface is nearly faced-on towards the camera perspective so that the offsets are difficult to see. Unlike other disks, MY lup models retain offsets highly similar to those inspected in the observation, which could be not interpreted by the same reason, as its size of extension is not comparable to HD 97047.

Meanwhile, we notice that discrepancies exist between the observed data and the models. The observation of HD 169142 shows a ring where the left and the right side is slightly brighter than top and bottom, and whereas in the model derived from HR 4796 A, we notice that the top is brighter than the bottom, with the two sides having approximately equal intensity. PDS 66 on the other hand is observed as more evenly distributed between the corona and outer ring, while the right side of the ring is vaguely darker than other sides, bearing a resemblance to the models where the dark color reveals at the right side as well. It is noted that the space between the host star and the inner edge of IM lup is vast in the observation than in the models, implying that gases and dust close to the center might have been evaporated or accreted onto the star. We have not yet incorporated photoevaporation and accretion in our model at the moment.

Furthermore, visual inspections show that MY lup fit to the observation to a large extent, because of the similar bright regions on the two sides of the central star and the disk offset. The model implemented with the phase function derived from HR 4796 A particularly resembles the data with an alike light distribution, yet the one implemented

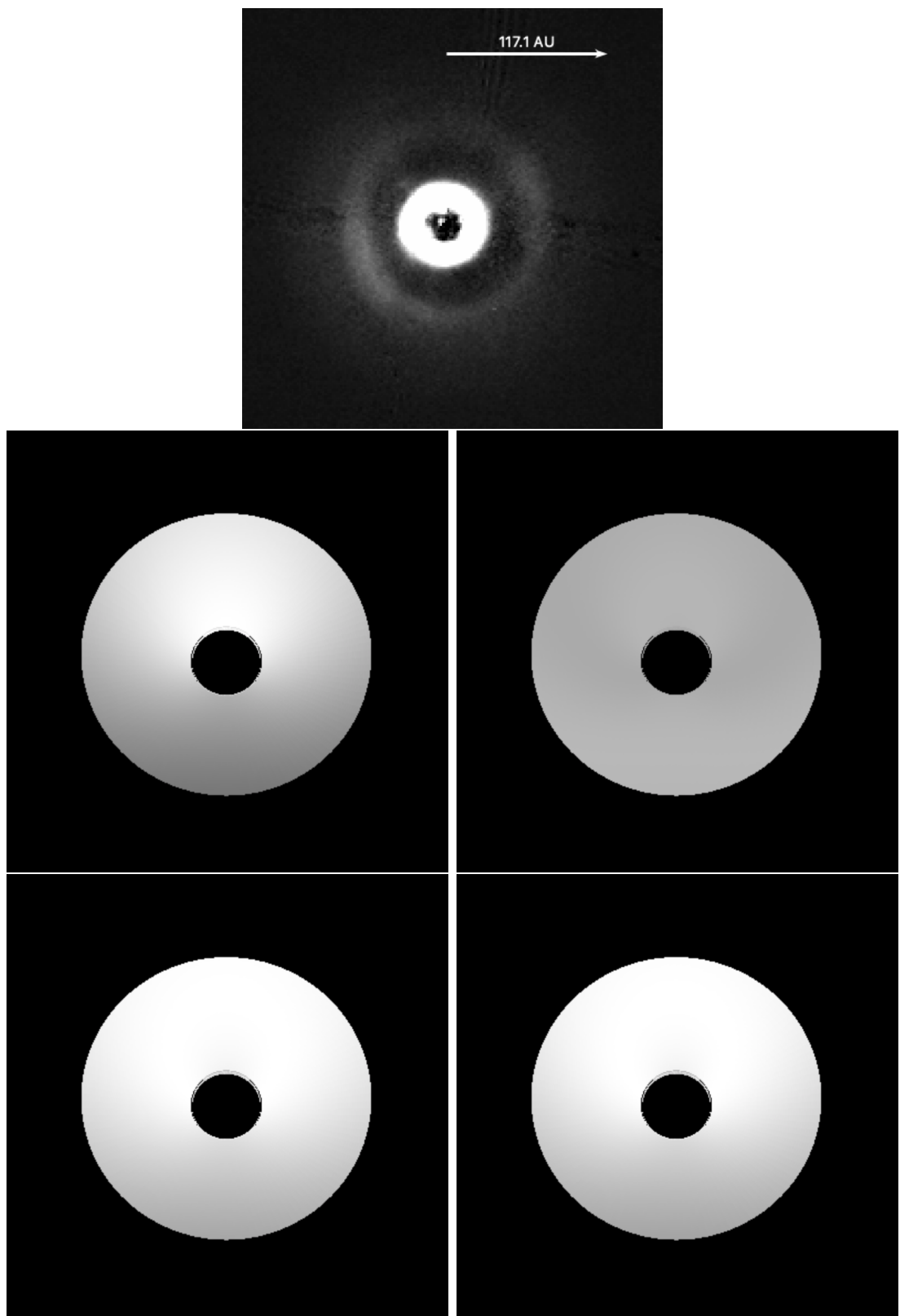


Figure 3.16: *Top:* observed image of HD 169142 at an inclination of 13 degrees. The size of the disk is measured to be 117.1 AU. *Clockwise from middle left:* same setup as the right panel of [Figure 3.12](#), [Figure 3.13](#), [Figure 3.15](#), and [Figure 3.14](#), respectively. All disk inclinations and separations have been adjusted to match with the observation.

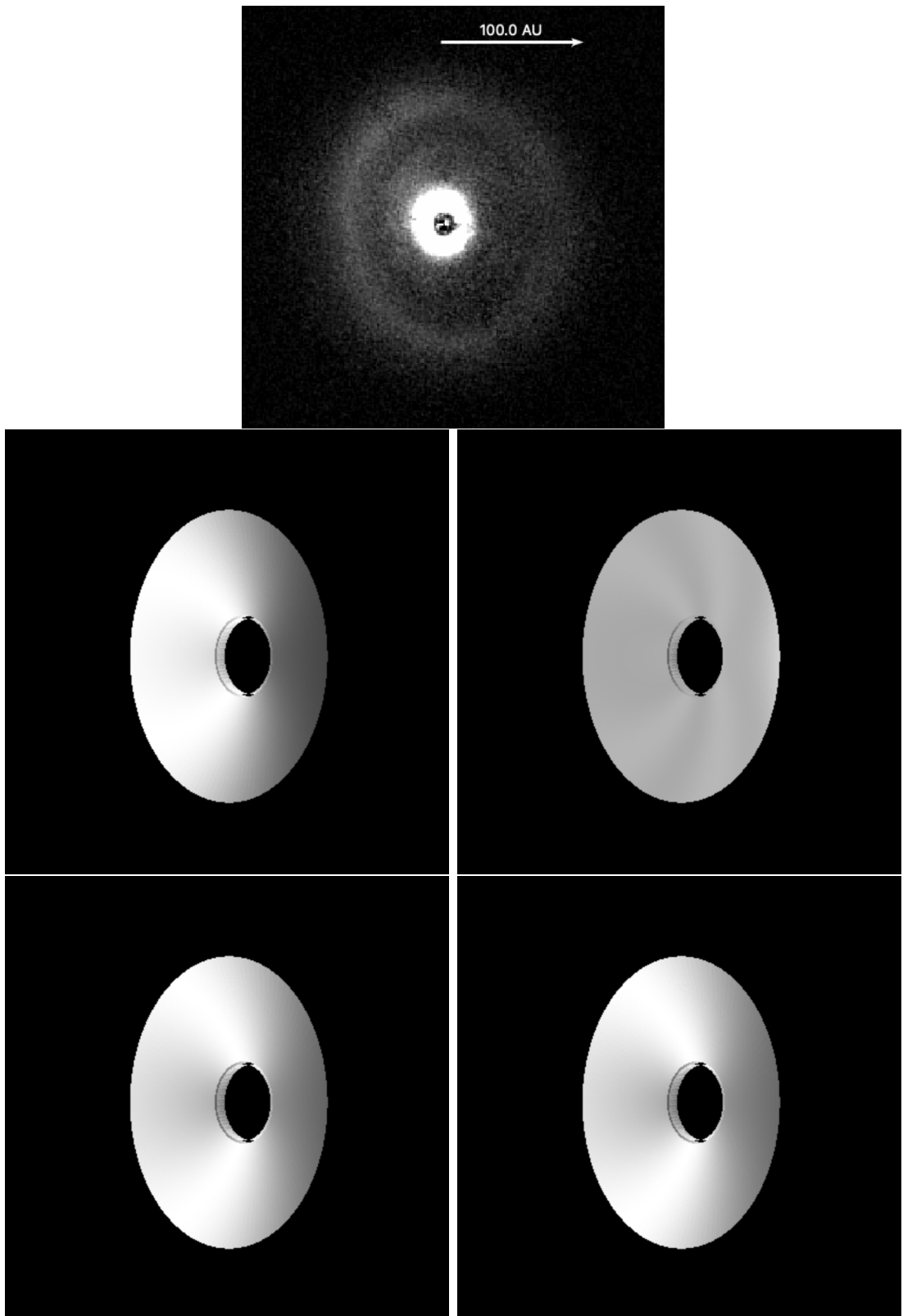


Figure 3.17: *Top*: observed image of PDS 66 at an inclination of 30.26 degrees. The size of the disk measured to be 100.0 AU. *Clockwise from middle left*: same as [Figure 3.16](#).

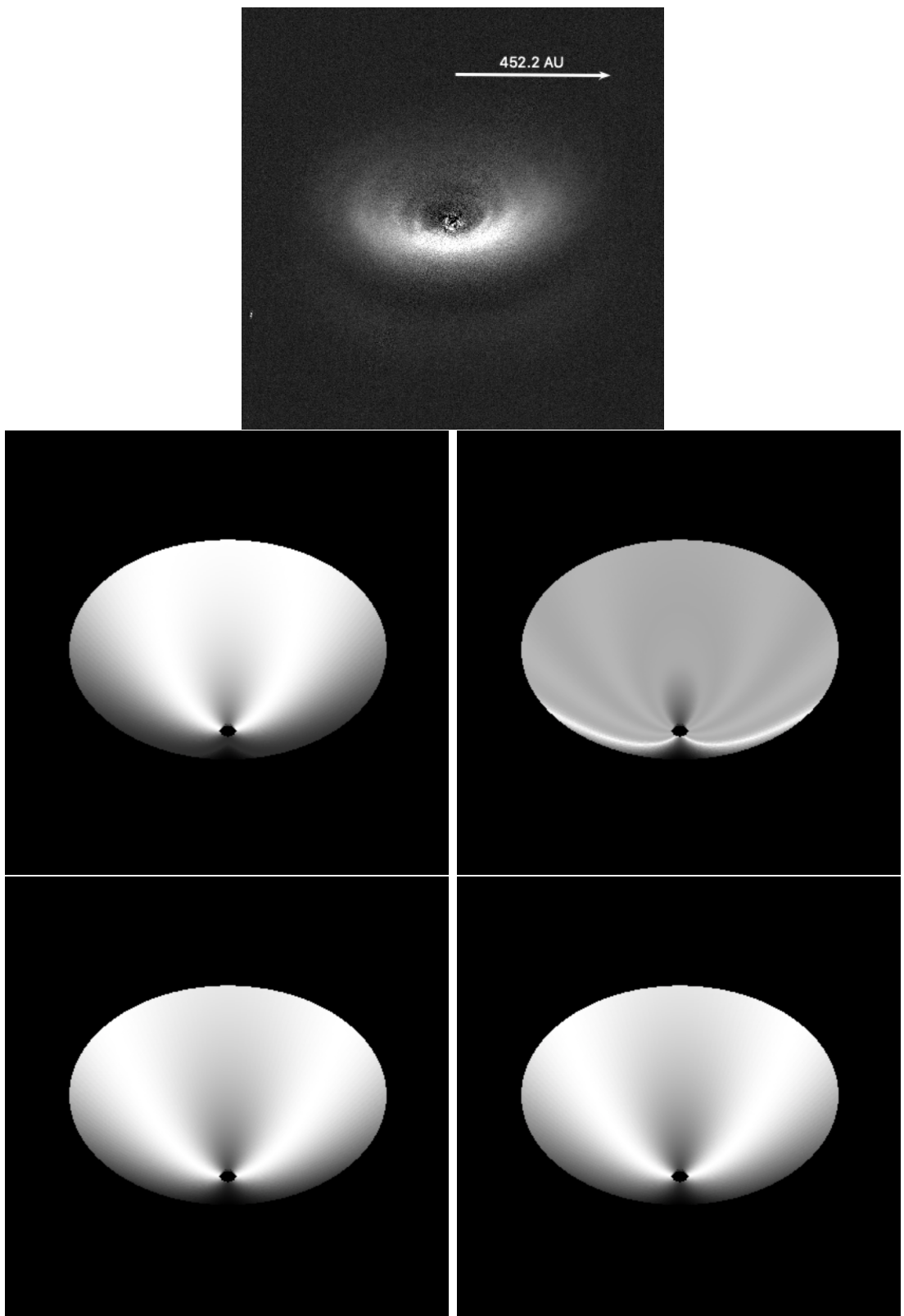


Figure 3.18: *Top:* observed image of IM lup at an inclination of 55 degrees. The size of the disk is measured to be 452.2 AU. *Clockwise from middle left:* same as Figure 3.16.

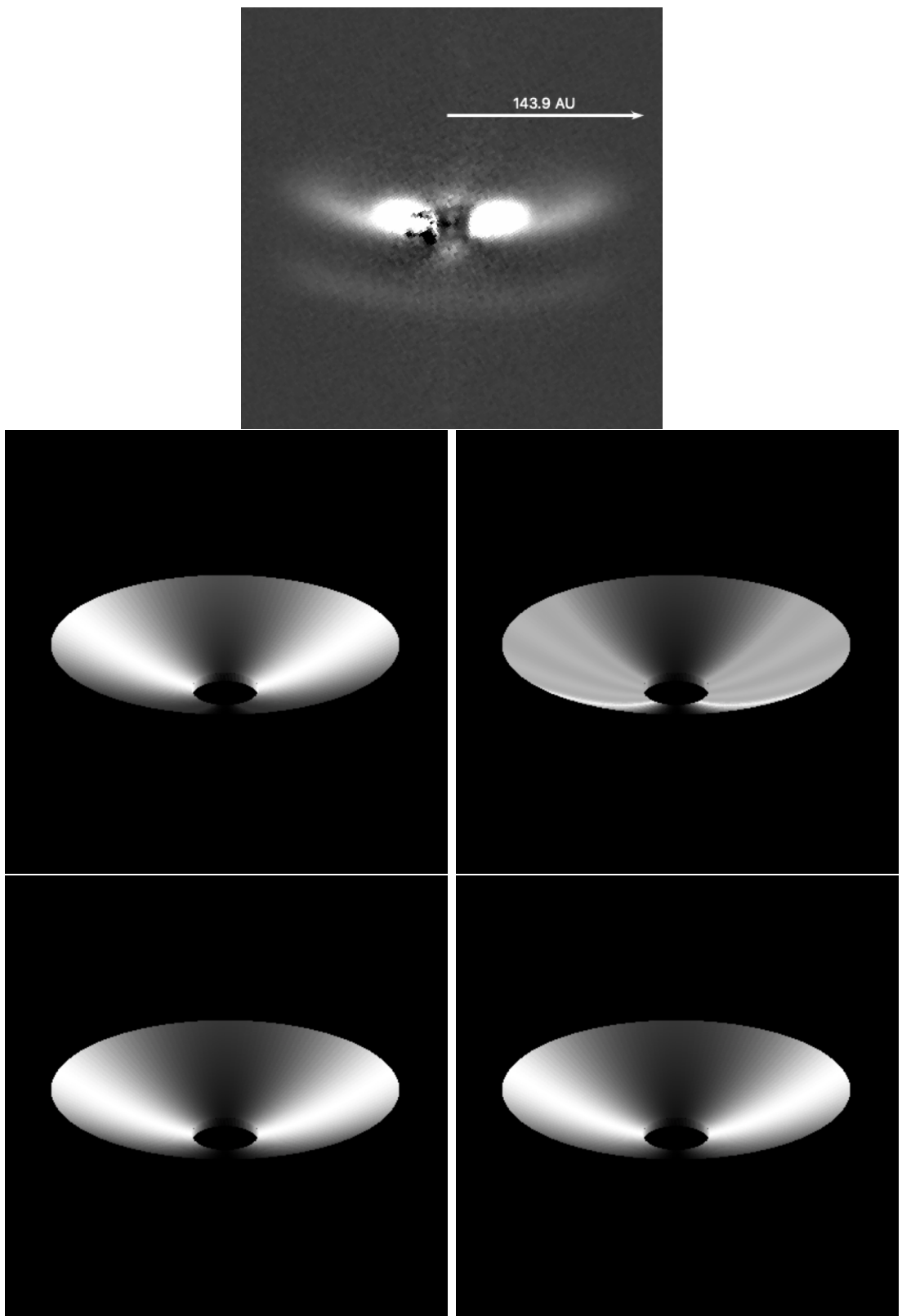


Figure 3.19: *Top*: observed image of MY lup at an inclination of 77 degrees. The size of the disk is measured to be 143.9 AU. *Clockwise from middle left*: same as [Figure 3.16](#).

with the phase function of HD 97064 looks very differently. An explanation could be that older disks aggregate more dust than young disks do, making them favorable to models with phase functions derived from disks closer to their ages. This is moderately verified by the forward scattering of IM lup, which is only apparent in the model of HD 97064 phase function. The forward and backward scatterings in the other three models are somewhat flipped compared to the observation. Similarly, the above-mentioned light distribution of PDS 66's surface brightness resembles slightly more the model with HR 4796 A phase function, though it is difficult to make the comparison as the observed image is quite faint. BCCA and BPCA models of these three disks are highly akin to the HR 4796 A model, which implies their preference for old disks. Nonetheless, the result of HD 169142 seems not agreeable with our statement. HD 169142 would be more favorable towards the HD 97048 model given its relatively young age, but they share only a limited amount of perceptible similarities. The model is not able to reproduce a relatively darker top of the inner ring. Since the outer ring in the observed image is barely visible, a full disk comparison to the model would be hard to achieve.

We have also categorized the disks based on their preferences towards certain models and their ages to better visualize the potential correlation between these aspects, as shown in [Figure 3.20](#). We notice that disks whose ages are less than ~ 7 Myrs favor

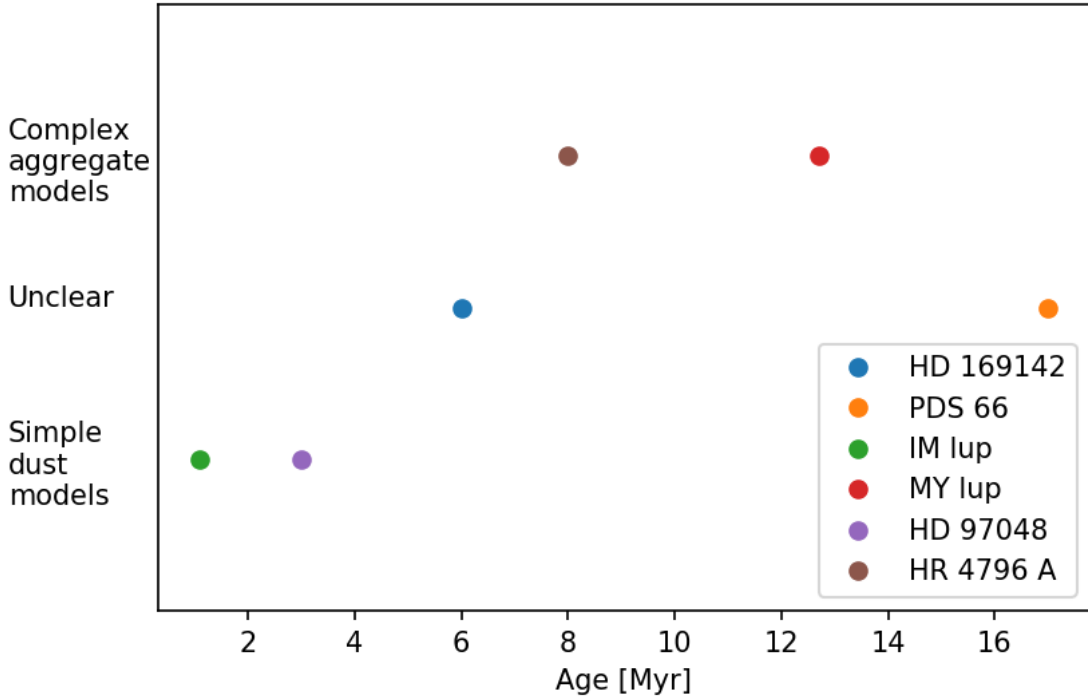


Figure 3.20: The map of disk fitness to certain types of models. Complex aggregate models refer to those described by phase functions derived from measurements of old debris disks, while simple dust models are fitted by phase functions of young gas-rich disks. Ambiguous disk models are placed into a separate group.

the simple dust models and those older than that age fit more closely to the complex aggregate models. However, two disk models remained equivocal. Possible explanations may include mismatched separation and height profiles, limited probing angles, or simply

insufficient amount of samples. No solid conclusion is drawn due to numerous questions left unanswered.

Our disk model ignores the limited resolution of telescopes. The height profile may not fit the actual disk as accurately as the actual measurement, but the model can at least provide a solid start to indicate similarities between basic dust grain. In principle, the model construction is still at the beginning stage, yet the fundamental structure has been established and future editions would only need minimal actions. For example, height profiles can be modified to fit more closely to the actual measurement with a few lines of commands. More details of the disk system, such as the stellar mass, age, star-forming regions, etc., can be added to increase the complexity so that the disk becomes more realistic. The idea of designing a web database including all observations conducted and published is indeed to satisfy this requirement. Ideally, combining the database and the model will provide easy access to various disk properties updated to the latest version.

Chapter 4

Conclusion

We inspect the surface brightness of circumstellar disks based on the scattered light of HD 97048 and comparisons with various disks. Through the JavaScript library `three.js`, we reconstruct the disks in accelerated graphical animation in 3D using the measured height profile from SPHERE Q_{phi} image and total intensity phase function. In order to account for the effect of polarization during the observation, a polarization efficiency (degree of polarization) computed from the Rayleigh single scattering polarization is multiplied with the total intensity, yielding the polarized intensity phase function. The polarization phase function is then applied to illuminate the disk in RGB channels.

To visualize the performance of the disk model, we utilize the observed phase functions of HR 4796 A, HD 97048, and simulated phase functions of the porous dust aggregate model. All phase functions are fitted with two and three-component HG functions and 7th-degree polynomials. The best-fit curves are taken to implement on the models. HD 97048 has been well reconstructed in the model as it shows a center offset and a stronger forward scattering than backward scattering, though the gap between the inner and outer ring has not been included yet.

We then examine HD 169142, PDS 66, IM lup, and MY lup, and seek for comparisons between the model and those captured images. Our model successfully reproduces the stronger scattering effects at high-inclination angles. Among all disks, MY lup reveals a high-level resemblance to our model fitted with the phase function calculated from HR 4796 A. We propose a hypothesis that disks prefer models with phase functions derived from observations of other disks at a similar age, yet this statement requires more experiments to verify.

The properties of disks could have huge impacts on their structures, compositions, and may even affect their evolutionary processes. A large number of studies have been carried out to decipher the relation between parameters and disks themselves. To link researches from different perspectives, we design a web database collecting all previous observations conducted and published to date. This catalog combines with a simple user interface easy to access and manage data from the administration. Future investigations of relations between different disk properties could benefit from the shortened time spent searching for data.

Both disk catalog and visualization are still at the beginning stage of development. More details will be included in the future so that the models are more close to reality. Additionally, we intend to add a set of interactive functions allowing the general audiences to participate in understanding circumstellar disks. Our project aims to serve as a bridge connecting scientists and the public and to provide dialogues in between.

Bibliography

- [1] J. Milli, A. Vigan, D. Mouillet, A. M. Lagrange, J. C. Augereau, C. Pinte, D. Mawet, H. M. Schmid, A. Boccaletti, L. Matrà, Q. Kral, S. Ertel, G. Chauvin, A. Bazzon, F. Ménard, J. L. Beuzit, C. Thalmann, C. Dominik, M. Feldt, T. Henning, M. Min, J. H. Girard, R. Galicher, M. Bonnefoy, T. Fusco, J. de Boer, M. Janson, A. L. Maire, D. Mesa, J. E. Schlieder, and SPHERE Consortium. Near-infrared scattered light properties of the HR 4796 A dust ring. A measured scattering phase function from 13.6° to 166.6°. *A&A*, 599:A108, March 2017.
- [2] Michiel Min. Modeling and interpretation of images. In *European Physical Journal Web of Conferences*, volume 102 of *European Physical Journal Web of Conferences*, page 00016, September 2015.
- [3] C. Ginski, T. Stolker, P. Pinilla, C. Dominik, A. Boccaletti, J. de Boer, M. Benisty, B. Biller, M. Feldt, A. Garufi, C. U. Keller, M. Kenworthy, A. L. Maire, F. Ménard, D. Mesa, J. Milli, M. Min, C. Pinte, S. P. Quanz, R. van Boekel, M. Bonnefoy, G. Chauvin, S. Desidera, R. Gratton, J. H. V. Girard, M. Keppler, T. Kopytova, A. M. Lagrange, M. Langlois, D. Rouan, and A. Vigan. Direct detection of scattered light gaps in the transitional disk around HD 97048 with VLT/SPHERE. *A&A*, 595:A112, November 2016.
- [4] Ryo Tazaki, H. Tanaka, T. Muto, A. Kataoka, and S. Okuzumi. Effect of dust size and structure on scattered-light images of protoplanetary discs. *MNRAS*, 485(4):4951–4966, June 2019.
- [5] C. A. Grady, G. Schneider, K. Hamaguchi, M. L. Sitko, W. J. Carpenter, D. Hines, K. A. Collins, G. M. Williger, B. E. Woodgate, Th. Henning, F. Ménard, D. Wilner, R. Petre, P. Palunas, A. Quirrenbach, III Nuth, J. A., M. D. Silverstone, and J. S. Kim. The Disk and Environment of a Young Vega Analog: HD 169142. *ApJ*, 665(2):1391–1406, August 2007.
- [6] Eric E. Mamajek, Michael R. Meyer, and James Liebert. Post-T Tauri Stars in the Nearest OB Association. *AJ*, 124(3):1670–1694, September 2002.
- [7] Henning Avenhaus, Sascha P. Quanz, Antonio Garufi, Sebastian Perez, Simon Casassus, Christophe Pinte, Gesa H. M. Bertrang, Claudio Caceres, Myriam Benisty, and Carsten Dominik. Disks around T Tauri Stars with SPHERE (DARTTS-S). I. SPHERE/IRDIS Polarimetric Imaging of Eight Prominent T Tauri Disks. *ApJ*, 863(1):44, August 2018.
- [8] J. E. Pringle. Accretion discs in astrophysics. *ARA&A*, 19:137–162, January 1981.

- [9] Jonathan P. Williams and Lucas A. Cieza. Protoplanetary Disks and Their Evolution. *ARA&A*, 49(1):67–117, September 2011.
- [10] B. Zuckerman. Dusty Circumstellar Disks. *ARA&A*, 39:549–580, January 2001.
- [11] G. Neugebauer, H. J. Habing, R. van Duinen, H. H. Aumann, B. Baud, C. A. Beichman, D. A. Beintema, N. Boggess, P. E. Clegg, T. de Jong, J. P. Emerson, T. N. Gautier, F. C. Gillett, S. Harris, M. G. Hauser, J. R. Houck, R. E. Jennings, F. J. Low, P. L. Marsden, G. Miley, F. M. Olnon, S. R. Pottasch, E. Raimond, M. Rowan-Robinson, B. T. Soifer, R. G. Walker, P. R. Wesselius, and E. Young. The Infrared Astronomical Satellite (IRAS) mission. *ApJ*, 278:L1–L6, March 1984.
- [12] Karen M. Strom, Stephen E. Strom, Suzan Edwards, Sylvie Cabrit, and Michael F. Skrutskie. Circumstellar Material Associated with Solar-Type Pre-Main-Sequence Stars: A Possible Constraint on the Timescale for Planet Building. *AJ*, 97:1451, May 1989.
- [13] David A. Weintraub, G. Sandell, and W. D. Duncan. Submillimeter Measurements of T Tauri and FU Orionis Stars. *ApJ*, 340:L69, May 1989.
- [14] Steven V. W. Beckwith, Anneila I. Sargent, Rolf S. Chini, and Rolf Guesten. A Survey for Circumstellar Disks around Young Stellar Objects. *AJ*, 99:924, March 1990.
- [15] Anneila I. Sargent and Steven Beckwith. Kinematics of the Circumstellar Gas of HL Tauri and R Monocerotis. *ApJ*, 323:294, December 1987.
- [16] C. R. O’dell and Zheng Wen. Postrefurbishment Mission Hubble Space Telescope Images of the Core of the Orion Nebula: Proplyds, Herbig-Haro Objects, and Measurements of a Circumstellar Disk. *ApJ*, 436:194, November 1994.
- [17] Paul T. P. Ho, James M. Moran, and Kwok Yung Lo. The Submillimeter Array. *ApJ*, 616(1):L1–L6, November 2004.
- [18] S. Marino, S. Perez, and S. Casassus. Shadows Cast by a Warp in the HD 142527 Protoplanetary Disk. *ApJ*, 798(2):L44, January 2015.
- [19] M. Benisty, A. Juhász, S. Facchini, P. Pinilla, J. de Boer, L. M. Pérez, M. Keppler, G. Muro-Arena, M. Villenave, S. Andrews, C. Dominik, C. P. Dullemond, A. Galienne, A. Garufi, C. Ginski, and A. Isella. Shadows and asymmetries in the T Tauri disk HD 143006: evidence for a misaligned inner disk. *A&A*, 619:A171, November 2018.
- [20] G. A. Muro-Arena, M. Benisty, C. Dominik, S. Facchini, M. Villenave, R. van Boekel, G. Chauvin, A. Garufi, T. Henning, M. Janson, M. Keppler, A. Matter, F. Ménard, T. Stolker, A. Zurlo, P. Blanchard, D. Maurel, O. Moeller-Nilsson, C. Petit, A. Roux, A. Sevin, and F. Wildi. Shadowing and multiple rings in the protoplanetary disk of HD 139614. *A&A*, 635:A121, March 2020.
- [21] R. van Boekel, Th. Henning, J. Menu, J. de Boer, M. Langlois, A. Müller, H. Avenhaus, A. Boccaletti, H. M. Schmid, Ch. Thalmann, M. Benisty, C. Dominik, Ch. Ginski, J. H. Girard, D. Gisler, A. Lobo Gomes, F. Menard, M. Min, A. Pavlov,

- A. Pohl, S. P. Quanz, P. Rabou, R. Roelfsema, J. F. Sauvage, R. Teague, F. Wildi, and A. Zurlo. Three Radial Gaps in the Disk of TW Hydrae Imaged with SPHERE. *ApJ*, 837(2):132, March 2017.
- [22] N. van der Marel, P. Cazzoletti, P. Pinilla, and A. Garufi. Vortices and Spirals in the HD135344B Transition Disk. *ApJ*, 832(2):178, December 2016.
- [23] Kevin Wagner, Ruobing Dong, Patrick Sheehan, Dániel Apai, Markus Kasper, Melissa McClure, Katie M. Morzinski, Laird Close, Jared Males, Phil Hinz, Sascha P. Quanz, and Jeffrey Fung. The Orbit of the Companion to HD 100453A: Binary-driven Spiral Arms in a Protoplanetary Disk. *ApJ*, 854(2):130, February 2018.
- [24] G. A. Muro-Arena, C. Ginski, C. Dominik, M. Benisty, P. Pinilla, A. J. Bohn, T. Moldenhauer, W. Kley, D. Harsono, T. Henning, R. G. van Holstein, M. Janson, M. Keppler, F. Ménard, L. M. Pérez, T. Stolker, M. Tazzari, M. Villenave, A. Zurlo, C. Petit, F. Rigal, O. Möller-Nilsson, M. Llored, T. Moulin, and P. Rabou. Spirals inside the millimeter cavity of transition disk SR 21. *A&A*, 636:L4, April 2020.
- [25] J. L. Beuzit, A. Vigan, D. Mouillet, K. Dohlen, R. Gratton, A. Boccaletti, J. F. Sauvage, H. M. Schmid, M. Langlois, C. Petit, A. Baruffolo, M. Feldt, J. Milli, Z. Wahhaj, L. Abe, U. Anselmi, J. Antichi, R. Barette, J. Baudrand, P. Baudoz, A. Bazzon, P. Bernardi, P. Blanchard, R. Brast, P. Bruno, T. Buey, M. Carbillet, M. Carle, E. Cascone, F. Chapron, J. Charton, G. Chauvin, R. Claudi, A. Costille, V. De Caprio, J. de Boer, A. Delboulbé, S. Desidera, C. Dominik, M. Downing, O. Dupuis, C. Fabron, D. Fantinel, G. Farisato, P. Feautrier, E. Fedrigo, T. Fusco, P. Gigan, C. Ginski, J. Girard, E. Giro, D. Gisler, L. Gluck, C. Gry, T. Henning, N. Hubin, E. Hugot, S. Incorvaia, M. Jaquet, M. Kasper, E. Lagadec, A. M. La-grange, H. Le Coroller, D. Le Mignant, B. Le Ruyet, G. Lessio, J. L. Lizon, M. Llored, L. Lundin, F. Madec, Y. Magnard, M. Marteaud, P. Martinez, D. Maurel, F. Mé-nard, D. Mesa, O. Möller-Nilsson, T. Moulin, C. Moutou, A. Origné, J. Parisot, A. Pavlov, D. Perret, J. Pragt, P. Puget, P. Rabou, J. Ramos, J. M. Reess, F. Rigal, S. Rochat, R. Roelfsema, G. Rousset, A. Roux, M. Saisse, B. Salasnich, E. Santam-brogio, S. Scuderi, D. Segransan, A. Sevin, R. Siebenmorgen, C. Soenke, E. Stadler, M. Suarez, D. Tiphène, M. Turatto, S. Udry, F. Vakili, L. B. F. M. Waters, L. We-ber, F. Wildi, G. Zins, and A. Zurlo. SPHERE: the exoplanet imager for the Very Large Telescope. *A&A*, 631:A155, November 2019.
- [26] Django Software Foundation. Django, April 2020. Available at [https://django-project.com](https://.djangoproject.com), version 3.0.5.
- [27] Caer McCabe. Catalog of circumstellar disks. <https://webdisks.jpl.nasa.gov/>.
- [28] A. Garufi, M. Benisty, P. Pinilla, M. Tazzari, C. Dominik, C. Ginski, Th. Henning, Q. Kral, M. Langlois, F. Ménard, T. Stolker, J. Szulagyi, M. Villenave, and G. van der Plas. Evolution of protoplanetary disks from their taxonomy in scattered light: spirals, rings, cavities, and shadows. *A&A*, 620:A94, December 2018.
- [29] Three.js Authors. Three.js, March 2020. Source code at <https://threejs.org>, stable release r114.
- [30] J.H. Seinfeld and S.N. Pandis. *Atmospheric Chemistry and Physics: From Air Pollution to Climate Change*. Wiley, 2016.

- [31] J W Hovenier M I Mishchenko and L (editors). Light scattering by nonspherical particles: Theory, measurements, and applications. *Measurement Science and Technology*, 11(12):1827–1827, nov 2000.
- [32] L. G. Henyey and J. L. Greenstein. Diffuse radiation in the Galaxy. *ApJ*, 93:70–83, January 1941.
- [33] Christopher C. Stark, Glenn Schneider, Alycia J. Weinberger, John H. Debes, Carol A. Grady, Hannah Jang-Condell, and Marc J. Kuchner. Revealing Asymmetries in the HD 181327 Debris Disk: A Recent Massive Collision or Interstellar Medium Warping. *ApJ*, 789(1):58, July 2014.
- [34] Matthew M. Hedman and Christopher C. Stark. Saturn’s G and D Rings Provide Nearly Complete Measured Scattering Phase Functions of Nearby Debris Disks. *ApJ*, 811(1):67, September 2015.
- [35] T. Stolker, C. Dominik, M. Min, A. Garufi, G. D. Mulders, and H. Avenhaus. Scattered light mapping of protoplanetary disks. *A&A*, 596:A70, December 2016.
- [36] Travis E. Oliphant. *A Guide to NumPy*. USA: Trelgol Publishing, 2006.
- [37] Pauli Virtanen, Ralf Gommers, Travis E. Oliphant, Matt Haberland, Tyler Reddy, David Cournapeau, Evgeni Burovski, Pearu Peterson, Warren Weckesser, Jonathan Bright, Stéfan J. van der Walt, Matthew Brett, Joshua Wilson, K. Jarrod Millman, Nikolay Mayorov, Andrew R. J. Nelson, Eric Jones, Robert Kern, Eric Larson, CJ Carey, İlhan Polat, Yu Feng, Eric W. Moore, Jake VanderPlas, Denis Laxalde, Josef Perktold, Robert Cimrman, Ian Henriksen, E. A. Quintero, Charles R Harris, Anne M. Archibald, Antônio H. Ribeiro, Fabian Pedregosa, Paul van Mulbregt, and SciPy 1. 0 Contributors. SciPy 1.0—Fundamental Algorithms for Scientific Computing in Python. *arXiv e-prints*, page arXiv:1907.10121, July 2019.
- [38] Kjetil Dohlen, Maud Langlois, Michel Saisse, Lucien Hill, Alain Origne, Marc Jacquet, Christophe Fabron, Jean-Claude Blanc, Marc Llored, Michael Carle, Claire Moutou, Arthur Vigan, Anthony Boccaletti, Marcel Carillet, David Mouillet, and Jean-Luc Beuzit. The infra-red dual imaging and spectrograph for SPHERE: design and performance. In Proc. SPIE, volume 7014 of *Society of Photo-Optical Instrumentation Engineers (SPIE) Conference Series*, page 70143L, July 2008.
- [39] Bruce Hapke. Bidirectional reflectance spectroscopy 7. The single particle phase function hockey stick relation. *Icarus*, 221(2):1079–1083, November 2012.
- [40] Ryo Tazaki, Hidekazu Tanaka, Satoshi Okuzumi, Akimasa Kataoka, and Hideko Nomura. Light Scattering by Fractal Dust Aggregates. I. Angular Dependence of Scattering. *ApJ*, 823(2):70, June 2016.
- [41] Y. Okada. Efficient numerical orientation averaging of light scattering properties with a quasi-Monte-Carlo method. *J. Quant. Spec. Radiat. Transf.*, 109:1719–1742, June 2008.